# Quantifying Thermal Infra-Red directional anisotropy using Master and Landsat-8 simultaneous acquisitions

Julien Michel, Olivier Hagolle, Simon J Hook, Jean-Louis Roujean, Philippe Gamet

# Quantifying Thermal Infra-Red directional anisotropy using Master and Landsat-8 simultaneous acquisitions

Julien Michel[a,*], Olivier Hagolle[a], Simon J. Hook[b], Jean-Louis Roujean[a], Philippe Gamet[a]

[a] *CESBIO, Université de Toulouse, CNES, CNRS, INRAE, IRD, UT3, 18 avenue Edouard Belin, BPI 2801, TOULOUSE Cedex 9, 31401, France*
[b] *Jet Propulsion Laboratory, California Institute of Technology, 4800 Oak Grove Drive, Pasadena, CA 91109, United States*

## Abstract

Satellite observations in the Thermal Infra-Red (TIR) domain provide valuable information on Land Surface Temperatures, Evapo-Transpiration and water use efficiency and are useful for monitoring vegetation health, agricultural practices and urban planning. By 2030, there will be 3 new high-resolution global coverage satellite TIR missions in space, all of them with fields of view larger than ± 30°. Directional anisotropy in TIR can affect the estimation of key application variables, such as temperature, and are typically studied by means of field campaigns or physical modelling. In this work, we have evaluated directional effects using simultaneous measurements from Landsat-8 and the ± 45° field of view MASTER airborne TIR sensor from NASA. Differences as high as 6K are observed in the surface temperatures derived from these simultaneous observations. Those differences are attributed to directional effects, with the greatest differences associated with hotspot conditions, where the solar and satellite viewing directions align. Five well studied parametric directional models have then been fitted to the temperature differences, allowing the amplitude of the measured directional effects to be reduced below 1K, with small variations between models. These results suggest that a simple correction for directional effects could be implemented as part of the ground segment processing for the upcoming missions.

*Keywords:* Thermal Infra-Red, Land Surface Temperature, MASTER, Landsat-8, Calibration, Anisotropy

*Corresponding author

*Email addresses:* julien.michel@cnes.fr (Julien Michel), olivier.hagolle@cnes.fr (Olivier Hagolle), simon.j.hook@jpl.nasa.gov (Simon J. Hook), jean-louis.roujean@univ-tlse3.fr (Jean-Louis Roujean), philippe.gamet@cnes.fr (Philippe Gamet)

## 1. Introduction

Earth observation from satellites provide radiometric data in the Thermal InfraRed (TIR) spectrum, namely in the 8-12 µm range, that further serve to estimate the Land Surface Temperature (LST), which is an Essential Climate Variable (ECV). LST is used in a broad range of applications, notably to estimate the surface energy balance (Anderson et al., 2008), and the evapo-transpiration (ET) (Price, 1982; Courault et al., 2005; Anderson et al., 2012), allowing to detect plant water stress (Boulet et al., 2015) and to monitor irrigation (Ishimwe et al., 2014).

A new generation of TIR sensors is foreseen to be launched in the coming years. They will have a high spatial resolution (ground sampling distance close to 60 meters at Nadir), and enhanced temporal resolution (every 3 days at equator, and even less at higher latitudes), and between 4 and 5 TIR channels, as well as other optical channels. Table 1 displays the main characteristics of these missions. The first on the agenda is TRISHNA (Thermal infraRed Imaging Satellite for High-resolution Natural resource Assessment) (Lagouarde et al., 2018), scheduled to be launched in 2026. This is a joint Indian and French mission developed by ISRO and CNES. It should be followed in 2027 by the Surface Biology and Geology (SBG) (Cawse-Nicholson et al., 2021), which is a joint mission between NASA and the Italian Space Agency (ASI). Last, the Land Surface Temperature Mission (LSTM) (Koetz et al., 2018) from the European Space Agency will be launched in 2029 for the first satellite and 2030 for the second one. All sensors from these TIR missions will be equipped with large Fields of View (FOV), in order to achieve both global coverage and short revisit time.

With maximum zenith angles reaching 30 to 40 degrees, it is expected that directional effects will affect the thermal images and the retrieval of LST by several Kelvins. They could therefore jeopardize the detection and monitoring of water stress as well as other downstream products (Mwangi et al., 2022). A normalization effort seems mandatory in order to reach the target accuracy of 1K for LST. For instance, the hotspot phenomena later introduced in section 1.1 will frequently contaminate TRISHNA, SBG and LSTM scenes in the tropics due to their overpassing time at noon. It is worth emphasizing that thanks to its orbit design, TRISHNA will provide a workaround to this

problem by observing the same scene with at least 3 different viewing angles within 8 days, whereas SBG and LSTM have opted for constant angles. In all cases, pre-processing of the Level 2 products should benefit from a correction of the directional effects. It is noteworthy that even if viewing angles of a single are constant for a given location, directional effects correction may still be required for the joint use of data from the three missions.

| **Satellite** | **Status** | **Agencies** | **Launch** | **Resolution** | **Revisit** | **FoV** |
|---|---|---|---|---|---|---|
| ASTER | End of life | JAXA | 1999 | 90 . | 16 days | 8.55° |
| Landsat-8 & 9 | Flying | NASA | 2013/21 | 100 m | 8d (2 sat) | 7.5° |
| ECOSTRESS | | NASA | 2018 | 38x69 m | irregular | 28° |
| TRISHNA | In prep. | CNES & ISRO | 2025 | 57 m | 3d (1 sat) | 34° |
| SBG | | NASA | 2027 | 60 m | <8d (1 sat) | 34° |
| LSTM | | ESA | 2029/31 | 37 m | 2d (2 sat) | 28° |

Table 1: Main features of high resolution TIR satellites. For missions with two satellites (2 sat), both launch years are mentioned.

### *1.1. Directional anisotropy in the TIR domain*

Satellite measurements of the LST inherently averages the temperature of visible elements within a pixel (Li et al., 2013). TIR directional effects are induced by changes in the proportions of those elements, within a pixel observed from different viewing angles. In structured landscapes, those elements can be divided into sunlit elements and shaded elements: when the sun and viewing directions get closer, proportion of visible shaded elements decreases, resulting in a larger proportion of hotter sunlit elements being observed. This artificially increases the observed temperature, forming the hotspot phenomenon (Jupp and Strahler, 1991). Another effect inducing TIR anisotropy is the gap fraction (Nilson, 1999), resulting from the change in proportions of elements with different emissivities, and thus different temperatures, under the same solar radiation. For instance, when observing a cropland, observations with large viewing angles will increase the proportion of vegetation observed, while at nadir, the proportion of soil observed will be higher. In general, for vegetation pixels such as canopies or croplands,

the gap fraction and hotspot effects result from the continuous change of proportions of sunlit and shaded leaves and sunlit and shaded background elements, which were modeled as a base shape kernel and a hotspot kernel, respectively, in Cao et al. (2021). More structured landscapes such as rows in croplands can emphasise both the hotspot and gap fraction effects, depending on the row orientation with respect to the satellite azimuth (Lagouarde et al., 2014). Finally, It is noteworthy that directional effects may also affect the Land Surface Emissivity (LSE) (Sobrino and Cuenca, 1999; Ermida et al., 2020).

Directional effects in the reflective domain have been well studied (Roujean et al., 1992; Wanner et al., 1995; Roujean, 2000) and model-based corrections are routinely applied to high resolution imagery such as Landsat and Sentinel-2 (Claverie et al., 2018). Directional effects in TIR domain were primarily investigated by means of simulations (Duffour et al., 2016; Cao et al., 2019; Bian et al., 2020, 2023) using physically-based radiative transfer codes such as 1D SCOPE (Yang et al., 2021) and 3D DART (Gastellu-Etchegorry, 1996; Gastellu-Etchegorry et al., 2017). Detailed DART mock-ups were built for various land-cover types. Parametric models (Ermida et al., 2018; Cao et al., 2021), are considered as the only mean to routinely correct for directional effects, and thereby be used in the ground segments processors. They were evaluated against SCOPE and DART simulations (Pinheiro et al., 2006; Bian et al., 2018; Cao et al., 2019), or by cross-comparison with field measurements(Duffour et al., 2016) and medium resolution LEO (Low Elevation Orbit) and GEO (geostationary) satellites with large FOVs (Vinnikov et al., 2012; Guillevic et al., 2013; Ren et al., 2014).

Current operating TIR High-Resolution (HR, 10 meter to 100 meter) satellite imagery is acquired by instruments with a narrow FOV, such as Landsat-8 (± 7.5°) or ASTER (± 8.5°), where directional effects do not have a significant impact on LST measurements. A noticeable exception is the ECOSTRESS mission flying onboard the International Space Station (ISS) (Fisher et al., 2020), with its wide FOV ( ± 30°). Currently, there is no systematic correction of directional effects in the level 2 data processing of ECOSTRESS (Hulley and Hook, 2018).

### *1.2. Main contributions*

Simulating directional effects is valuable to understand the underlying physics, and to evaluate parametric models in a controlled environment. Simulations however have a limited variability with respect to the natural landscape that will be observed by a global coverage satellite mission. Databases of in situ measurements also lack sufficient diversity as they focus on a few plant species and land-cover types over selected geographic areas. Lower resolution (larger area) pixels from LEO and GEO satellites TIR images are a good complement to theoretical studies and field campaigns but their large pixels may include different types of landscapes whereas forthcoming higher resolution TIR missions will focus on a finer scale.

This work aims to assess a directional error budget in preparation of up-coming high spatial resolution TIR missions by utilizing available Landsat-8 imagery (Roy et al., 2014) combined with near simultaneous observations from the MODIS/ASTER airborne simulator (MASTER) (Hook et al., 2001). Evidences of directional behavior are identified and compared to several well-established directional models from the literature.

Landsat-8 is the well-known Earth-observation satellite from the Landsat series, providing a global coverage of the globe with a 16-days revisit since 2013. Landsat-8 has a TIR sensor resolution of 100 meters, though level 1 and 2 products further interpolate LST products to 30 meters. The Landsat-8 FOV is quite narrow, as its maximum View Zenith Angle (VZA) is 7.5°, and LST maps will therefore be considered as acquired under near Nadir conditions in this study. MASTER is an airborne sensor jointly developed by Ames Research Center (ARC), Jet Propulsion Laboratory (JPL), and the EROS Data Center to support algorithms development, calibration and validation for the ASTER and MODIS teams. The MASTER instrument has 50 channels in the 0.4 - 13 µm range, with 10 bands in the TIR wavelength range, with a large FOV (maximum VZA of 42.5°). It has been regularly flown since 1998, providing more than 658 days of acquisition. Spatial resolution ranges from 5 meters to 50 meters depending on the aircraft flight altitude. While Landsat-8 can provide near Nadir observations, MASTER fully covers the spatial resolution and VZA of the up-coming HR TIR missions listed in table 1. Though ECOSTRESS could also be considered, its FOV ( 28°)

does not cover the full FOV of the up-coming missions. Moreover, ECOSTRESS has a very large swath, and a single Landsat-8 scene only covers a fraction of the VZAs of ECOSTRESS. MASTER being an airborne sensor, it covers the full range of VZA in a very narrow swath that fits completely into a Landsat-8 image.

The remainder of this paper is organised as follows. Section 2 presents the matching methodology, the data processing, as well as the directional models and models fitting procedure. Section 3 presents LST comparison statistics for each match, the evidences of the directional effects and the performances of directional models fitted on the data. Section 4 discusses the limitations and possible follow-up to this study, and section 5 summarizes the results and future work.

## 2. Materials and methods

### *2.1. Matching methodology*

The full MASTER archive metadata has been kindly provided by JPL, and Landsat-8 collection 2 level 2 archive metadata (as of 2022.02.17) has been downloaded from the Land Processes DAAC. From these data, all pairs of MASTER and Landsat-8 products acquired during day-time, on the same date, with acquisition times within 10 minutes of each other, and with an overlap of respective bounding boxes no less than 50% have been selected.

Using this search process, 52 matches were identified, for which the Landsat-8 overpass occurs during MASTER track flight. Those 52 matches correspond to 24 unique MASTER tracks since one track can correspond to two Landsat-8 product. Among those 52 matches, 7 MASTER tracks are missing in the archive, which invalidates 17 pairs. This leaves 35 pairs for which both Landsat-8 products and MASTER L1B (radiance at sensor) and L2 (derived LST and emissivities) products are available. Among those, there are 16 pairs for which the processing described in section 2.2 does not yield a valid difference image, because of cloud occurrences or insufficient swath final overlap. Table 2 gives the products references of all valid pairs used in this study. As shown in figure 1, all sites are located in California or nearby. Figure 2 shows a detailed map view of valid overlapping area for each MASTER track, with the overlap

of the second Landsat-8 image in blue when applicable. This map shows that for most of the tracks (3, 4, 6, 10, 12), the second Landsat-8 does not bring additional coverage, to the noticeable exception of tracks 8 and 9.

| Id | MASTER track id | Landsat L2 product id |
|---|---|---|
| 1 | 2013-03-29_18:06:53 | LC08_L2SP_038037_20130329_20200912_02_T1 |
| 2 | 2013-04-11_18:14:46 | LC08_L2SP_041036_20130411_20200912_02_T1 |
| 3a | 2013-05-22_18:13:09 | LC08_L2SP_040036_20130522_20200913_02_T1 |
| 3b | 2013-05-22_18:13:09 | LC08_L2SP_040037_20130522_20200913_02_T1 |
| 4 | 2013-12-05_18:23:35 | LC08_L2SP_043035_20131205_20200912_02_T1 |
| 5a | 2014-03-31_18:11:16 | LC08_L2SP_039035_20140331_20200911_02_T1 |
| 5b | 2014-03-31_18:11:16 | LC08_L2SP_039036_20140331_20200911_02_T1 |
| 6a | 2014-04-14_18:27:14 | LC08_L2SP_041036_20140414_20200911_02_T1 |
| 6b | 2014-04-14_18:27:14 | LC08_L2SP_041037_20140414_20200911_02_T1 |
| 7 | 2014-04-28_18:22:43 | LC08_L2SP_043035_20140428_20200911_02_T1 |
| 8a | 2014-06-06_18:25:35 | LC08_L2SP_044033_20140606_20200911_02_T1 |
| 8b | 2014-06-06_18:25:35 | LC08_L2SP_044034_20140606_20200911_02_T1 |
| 9a | 2014-10-21_18:35:15 | LC08_L2SP_043034_20141021_20200910_02_T1 |
| 9b | 2014-10-21_18:35:15 | LC08_L2SP_043035_20141021_20200911_02_T1 |
| 10a | 2015-05-28_18:13:05 | LC08_L2SP_040036_20150528_20200909_02_T1 |
| 10b | 2015-05-28_18:13:05 | LC08_L2SP_040037_20150528_20200909_02_T1 |
| 11 | 2018-06-19_18:28:30 | LC08_L2SP_042034_20180619_20200831_02_T1 |
| 12a | 2021-03-30_18:32:40 | LC08_L2SP_043033_20210330_20210409_02_T1 |
| 12b | 2021-03-30_18:32:40 | LC08_L2SP_043034_20210330_20210409_02_T1 |

Table 2: List of valid MASTER and Landsat-8 pairs

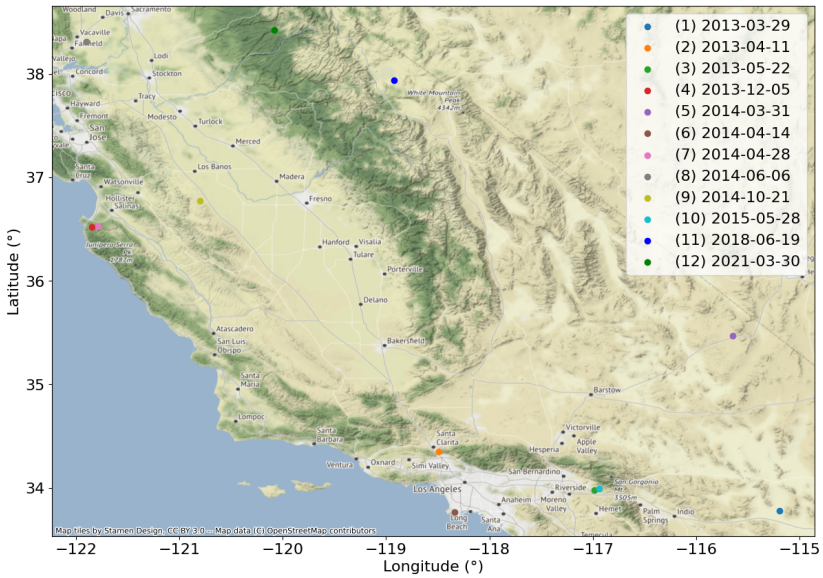


Figure 1: Location of the 12 MASTER tracks that have been matched to near simultaneous Landsat-8 acquisitions

## 2.2. *Data Processing*

### 2.2.1. *Product downloads*

Landsat-8 products have been downloaded from the collection 2 level 2 archive from the EarthExplorer portal[1]. MASTER L1B products (radiances and viewing angles), as well as L2 products (LST and geo-location grids) have been requested on the MASTER website[2]. Landsat-8 viewing angles have been computed by using a C program publicly available on USGS website[3].

### 2.2.2. *Target variables*

*Surface Brightness Temperature (SBT).* Both mission output LST and LSE maps. But they differ in the way those variables are estimated. On Landsat-8, there is a single

[1] https://earthexplorer.usgs.gov/, consulted on 2023.03.01

[2] https://masterprojects.jpl.nasa.gov/, consulted on 2023.03.01

[3] https://www.usgs.gov/landsat-missions/solar-illumination-and-sensor-viewing-angle-coefficient-file, consulted on 2022.09.12

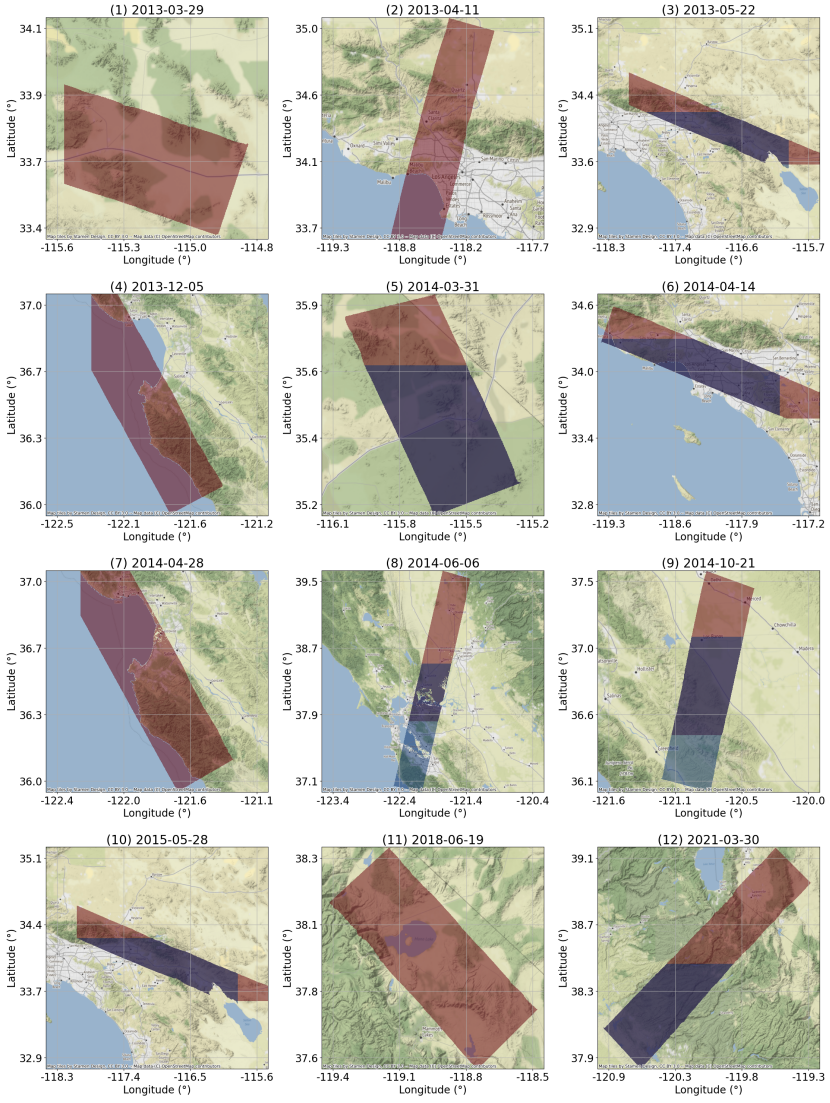


Figure 2: Detailed view of the overlapping MASTER tracks and Landsat-8 near simultaneous acquisitions. When two Landsat-8 images match a given track, the first image (a) is displayed in red and second image (b) in blue.

usable TIR band (B10, 10.6 - 11.19 µm), which prevents a joint estimation of LST and LSE. LSE is therefore derived by modulating the LSE from the ASTER Global Emissivity Database (Hulley et al., 2015) with the Normalized Difference Index (NDVI) and Snow Difference Index (NDSI) measured by Landsat-8. Various rules are applied to clamp emissivity values in corner cases. One important thing to note is that any emissivity lower than 0.6 is considered invalid and flagged as missing data. LST is then obtained by inverting the radiative transfer equation 1, with the atmospheric transmittance, upwelled and downwelled radiance estimated using (MODerate resolution atmospheric TRANsmission (MODTRAN) (Berk et al., 2014), Modern-Era Retrospective analysis for Research and Applications, Version 2 (MERRA-2) (Gelaro et al., 2017) and data from he GEOS-5 FP-IT Atmospheric Data Assimilation System (GEOS-5 ADAS) (Malakar et al., 2018).

$$L_\lambda(\theta) = [\epsilon_\lambda B_\lambda(T_s) + (1-\epsilon_\lambda)L_\lambda^\downarrow]\tau_\lambda(\theta) + L_\lambda^\uparrow(\theta) \tag{1}$$

where $L_\lambda(\theta)$ is the at sensor radiance, $\lambda$ is the wavelength, $\theta$ is the observation angle, $\epsilon_\lambda$ the surface emissivity, $T_s$ is the Surface Temperature, $L_\lambda^\downarrow$ is the downwelled radiance, $\tau_\lambda(\theta)$ is the atmospheric transmittance, $L_\lambda^\uparrow(\theta)$ is the upwelled radiance and $B_\lambda(T_s)$ is the Planck function defined in equation 2.

$$B_\lambda(T_s) = \frac{2hc^2}{\pi\lambda^5\left(\exp^{\frac{hc}{k\lambda T_s}}-1\right)} = \frac{C_1}{\lambda^5\left(\exp^{\frac{C_2}{\lambda T_s}}-1\right)} \tag{2}$$

Where $h = 6.63\times10^{-34}Ws^2$ (Planck constant), $c = 2.99\times10^8 ms^{-1}$ (speed of light), $k = 1.38\times10^{-23}WsK^{-1}$ (Boltzmann constant), $C_1 = 2\pi hc^2 = 3.74\times10^{-16}Wm^2$ (first radiative constant) and $C_2 = hc/k = 1.44\times10^4\mu mK$ (second radiative constant).

MASTER, on the other hand, uses the ASTER TES algorithm to retrieve LST values (Hook et al., 2011), using MODTRAN radiative transfer code and atmospheric parameters the Global Data Assimilation System (GDAS) products from the National Center for Environmental Prediction (NCEP). Those parameters are optimized for a flight altitude of 20 kilometers. Level 2 products include LST estimates as well emissivity estimates for channels 43, 44, 47, 48 and 49.

Since the algorithms for the separation of emissivity and LST are different, those

two variables may exhibit differences that are not related to directional effects. In order to limit the impact of those differences, this study recomputes the Surface Brightness Temperature (SBT), which corresponds to the temperature of a black-body emitting the same surface radiance, for both sensors, by means of equation 3, where $\lambda = 10.9\mu m$ (center wavelength of Landsat-8 B10 band).

$$\mathrm{SBT} = B_{\lambda}^{-1}(emis * B_{\lambda}(LST)) \tag{3}$$

Note that equation 3 is only changing the balance between already estimated emissivities and LST, under the same radiative transfer budget.

*Equivalent Landsat-8 emissivity from MASTER.* MASTER channels 47 and 48 overlap Landsat-8 B10 spectral sensitivity response, as shown in figure 3. Since the overlaps are significant, an equivalent Landsat-8 B10 emissivity is derived from MASTER, by means of linear combination of emissivities of channel 47 and 48, as shown in equation 4 to 6. The weights of the linear combinations are derived from the integration of the product of spectral sensitivities response, which correspond to the green and orange areas in figure 3. Weights are given in equation 7. This equivalent emissivity will be used as the MASTER emissivity throughout this study.

$$\epsilon^{*} = \frac{w_{47}}{w_{47} + w_{48}}\epsilon_{47} + \frac{w_{48}}{w_{47} + w_{48}}\epsilon_{48} \tag{4}$$

$$w_{47} = \int_{\lambda} SRS_{B10}^{landsat-8}(\lambda) * SRS_{47}^{MASTER}(\lambda) \tag{5}$$

$$w_{48} = \int_{\lambda} SRS_{B10}^{landsat-8}(\lambda) * SRS_{48}^{MASTER}(\lambda) \tag{6}$$

$$\frac{w_{47}}{w_{47} + w_{48}} = 0.605, \quad \frac{w_{48}}{w_{47} + w_{48}} = 0.395 \tag{7}$$

### *2.2.3. Geometric processing*

In order to compare measurements from products from the different sensors, they need to be first resampled to a common cartographic sampling grid. For each pair, this grid is defined using the Universal Transverse Mercator (UTM) cartographic projection of the Landsat-8 image of the pair. The sampling grid is defined according to the overlap area of the two products, and aligned to a multiple of the target resolution. The

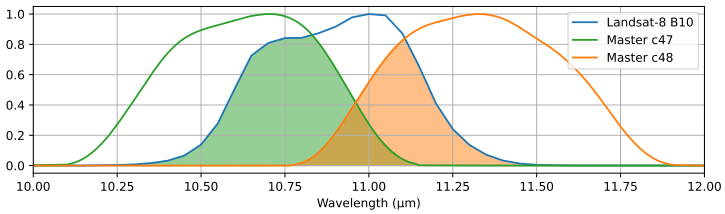


Figure 3: Spectral Sensitivity Response of Landsat-8 and MASTER overlapping Thermal Infra-Red spectral bands

target resolution is set to 100 meters for pairs of Landsat-8 and MASTER images, since the native resolution of Landsat-8 TIR bands is 100 meter.

Landsat-8 resampling is achieved through an averaging filter, which should not incur any aliasing artifacts since the Landsat-8 LST and emissivity measurements are resampled at 30 meters resolution through bicubic interpolation. MASTER being a whisk-broom sensor, its sampling is regular in viewing angle and therefore irregular in ground geometry: both spacing between pixels and pixel size increase with the viewing angle. Resampling of those measurements to the target ground grid is achieved by means of Gaussian Weights Averaging (GWA), as described in equation 8, through its implementation in the *pyresample* library (Hoese et al., 2022):

$$V(x,y) = \sum_{i \in N(x,y)} e^{\frac{-(x-x_i)^2+(x-x_i)^2}{\sigma^2}} V_i \tag{8}$$

Where $(V_i, x_i, y_i)$ are swath samples of measurement V at location $(x_i, y_i)$, $N(x,y)$ are the N nearest neighbours of target ground location $(x,y)$, and $\sigma$ is a user-defined parameter, which is set using equation 9:

$$\sigma(r,R,mtf) = \frac{max(r,R)}{\pi} \sqrt{-2ln(mtf)} \tag{9}$$

Where $mtf$ is the value of the Modulation Transfer Function (MTF) at Nyquist cut-off frequency, allowing to trade level of blur and aliasing off, $r$ is the native sensor resolution and $R$ is the target resolution. In this work, MTF has been set to 0.1, which yields a sigma of 68.3 meters for MASTER.

Given that all MASTER flights occurred at an altitude between 19 702 meters and 20 088 meters, depending on the position in the swath and the flight azimuth, the output

100 meter pixels cover between 12.5 milliradians and 23.7 milliradians of the initial instantaneous MASTER FOV, which is 2.25 milliradians per pixel.

#### 2.2.4. *Quality filtering*

Only samples that are marked as clear and not flagged as water or snow in the Pixel Quality Assessment mask from the Level 2 Landsat-8 products are kept for analysis. No additional quality filtering is performed on the MASTER side.

#### 2.2.5. *Angular distance*

Let $(\theta_0, \phi_0)$ and $(\theta_1, \phi_1)$ denote two viewing directions by their zenith angle $\theta$ and azimuth angle $\phi$.The angle between those two viewing directions is given by equation 10:

$$D_{ang}(\theta_0, \phi_0, \theta_1, \phi_1) = \arccos\left(\sin(\theta_0) \times \sin(\theta_1) \times \cos(\phi_0 - \phi_1) + \cos(\theta_0) \times \cos(\theta_1)\right) \quad (10)$$

This distance is used in this work to measure proximity to hotspot conditions, as well as to measure distance between MASTER and Landsat-8 viewing directions.

### 2.3. *Directional parametric models*

Four models investigated by Cao et al. (2019) have been used in this work: the Ross-Li model (Roujean et al., 1992; Wanner et al., 1995; Ren et al., 2014), the LSF-Li model (Su et al., 2002), the Vinnikov model (Vinnikov et al., 2012) and the RL model (Roujean, 2000; Lagouarde and Irvine, 2008). In addition to those models, we also investigated the LSF-RL model from Cao et al. (2021). Models are presented in table 3, where $\theta_v$ (resp. $\theta_s$) is the view (resp. solar) zenith angle, and $\Delta_\phi$ denotes the difference between solar and view azimuth angle. Unless stated otherwise, remaining notations and kernel expressions will be those from Cao et al. (2019). The full kernel functions are not provided here for the sake of conciseness. All models $m$ will be expressed as stated in equation 11, with $k_0, ..., k_n$ being the free parameters of the model:

$$T(\theta_v, \theta_s, \Delta_\phi) = m(\theta_v, \theta_s, \Delta_\phi, k_0, ..., k_n) \times T_{Nadir} \quad (11)$$

For the sake of consistency with the other models, the Roujean-Lagouarde (RL) kernel has been rewritten as equation 12:

$$K_{RL}(\theta_v, \theta_s, k_{hs}) = \frac{e^{-k_{hs}f} - e^{-k_{hs}f_n}}{1 - e^{-k_{hs}f_n}} \tag{12}$$

with $f$ and $f_n$ as written in Cao et al. (2019) (eq. 13 and 14). This mainly moves the original $\Delta_T$ parameter out of the kernel formulation, in order to use it as a kernel coefficient in table 3. It must be stressed that the RL model is the only one that does not have a volumetric kernel, but only a geometric kernel. The LSF-RL complement the RL model with the LSF volumetric kernel. To make that more obvious, in table 3, the parameter $k_0$ always represents the isotropic contribution, while $k_1$ stands for the coefficient of the volumetric kernel (and therefore the RL model has no $k_1$ parameter), and $k_2$ is the coefficient of the geometric or hotspot kernel. The hotspot width parameter inside the exponential in 12 is labelled $k_{hs}$, and it should be noted that the RL and LSF-RL models are the only models with parameters non-linearity.

| **Model** | Iso | Volumetric | Geometric / Hotpsot |
|---|---|---|---|
| Ross-Li | $k_0$ | $+ k_1 K_{RossThick}(\theta_v, \theta_s, \Delta_{phi})$ | $+k_2 K_{LiSparseR}(\theta_v, \theta_s, \Delta_{phi})$ |
| LSF-Li | $k_0$ | $+ k_1 K_{lsf}(\theta_v, \theta_s, \Delta_{phi})$ | $+k_2 K_{LiDenseR}(\theta_v, \theta_s, \Delta_{phi})$ |
| Vinnikov | $k_0$ | $+ k_1 K_{emis}(\theta_v, \theta_s, \Delta_{phi})$ | $+k_2 K_{solar}(\theta_v, \theta_s, \Delta_{phi})$ |
| RL | $k_0$ | | $+ k_2 K_{RL}(\theta_v, \theta_s, \Delta_{phi}, k_{hs})$ |
| LSF-RL | $k_0$ | $+ k_1 K_{lsf}(\theta_v, \theta_s, \Delta_{phi})$ | $+ k_2 K_{RL}(\theta_v, \theta_s, \Delta_{phi}, k_{hs})$ |

Table 3: Formulations of the five directional models from Cao et al. (2019) as well as of the LSF-RL model from Cao et al. (2021) investigated in this work

The fitting of model parameters on the data has been performed by ordinary Least-Squares as stated in equation 13:

$$\min_{(k_0,k_1,k_2,k_{hs})} \| m(\theta_v, \theta_s, \Delta_{phi}, k_0, ..., k_{hs}) \times T_{Nadir} - T_{Dir}(\theta_v, \theta_s, \Delta_{\phi}) \|^2 \tag{13}$$

where Landsat-8 SBT is used as $T_{Nadir}$ and MASTER SBT is used as $T_{Dir}$. Parameters $k_0$, $k_2$ and $k_{hs}$ are assumed to be strictly positive, and in Cao et al. (2019) the authors observe that $k_1$ is always negative. Additionally, $k_{hs}$ can not equal 0 in or-

der to avoid a null denominator in the exponential fraction. In order to enforce those constraints while still using unconstrained least-squares fitting, the models have been re-parametrized with exponential, and a small offset of 1e-6 has been added to $k_{hs}$ to avoid the under-determination around 0, as shown in equation 14:

$$k_0 = e^{k'_0}, \quad k_1 = -e^{k'_1}, \quad k_2 = e^{k'_2}, \quad k_{hs} = 1e-6 + e^{k'_{hs}} \tag{14}$$

Optimization has been performed using the Levenberg-Marquardt algorithm implemented in scipy (Virtanen et al., 2020). Initial values have been set to 1. for $k_0$, 0.01 for $k_1$ and $k_2$, which corresponds to a variation of SBT of 1% that is consistent with the observations in the dataset, and 1 for $k_{hs}$, where $k_0$, $k_1$, $k_2$ and $k_{hs}$ defined in table 3.

### *2.4. Land-cover analysis*

According to the literature, Land cover is one of the main drivers for TIR directional anisotropy, as both gap fraction and hotspot effects are driven by the structure of the landscape, and in particular, of the vegetation. In order to provide insights on the land-cover classes covered by each of the tracks, five high level classes have been extracted from the Copernicus Global Land Service maps at 100 meter resolution (Tsendbazar et al., 2021). This land cover source has been selected because it is available as open-data, it covers the area of interest and provides several years of land cover maps covering the observation period. Maps from Copernicus GLS only cover years 2015 to 2019, whereas MASTER tracks cover years2013 to 2021, therefore tracks prior to 2015 have been assigned the 2015 land cover, while tracks posterior to 2019 have been assigned the 2021 land cover, under the assumption that land cover only marginally changes from one year to another, especially for high level classes. High level classes are aggregated from the land-cover maps as described in table 4. Furthermore, since vegetation can be at different stages of growth depending on plant type and season, the cropland, low vegetation and forests classes have been further stratified according to the Normalized Difference Vegetation Index (NDVI) (Kriegler et al., 1969) computed from Landsat-8 in three sub-classes : low NDVI (between 0 and 0.2), intermediate NDVI (between 0.2 and 0.6), and high NDVI (greater than 0.6).

| High level class | Copernicus Global Land Service classes (label) |
|---|---|
| **Urban** | Urban / built up (50) |
| **Bare** | Bare / sparse vegetation (60) |
| **Croplands** | Cultivated and managed vegetation/agriculture (cropland) (40) |
| **Low vegetation** | Shrubs (20) |
| | Herbaceous vegetation (30) |
| | Herbaceous wetland (90) |
| | Moss and lichen (100) |
| **Forests** | Closed forest, evergreen needle leaf (111) |
| | Closed forest, evergreen, broad leaf (112) |
| | Closed forest, deciduous needle leaf (113) |
| | Closed forest, deciduous broad leaf (114) |
| | Closed forest, mixed (115) |
| | Closed forest, unknown (116) |
| | Open forest, evergreen needle leaf (121) |
| | Open forest, evergreen broad leaf (122) |
| | Open forest, deciduous needle leaf (123) |
| | Open forest, deciduous broad leaf (124) |
| | Open forest, mixed (125) |
| | Open forest, unknown (126) |

Table 4: The five high level class derived from class aggregation of the Copernicus Global Land Service classes

Table 5 gives the proportions of each classes for each analysed MASTER track. All proportions are given in percentage of the total number of available pixels. In this table, it can be noted that low vegetation and croplands seldom reach the highest NDVI strata, while forests have intermediate to high NDVI, which is expected and advocate for the consistency between the derived land-cover maps and the observed landscapes. Track (1) is mostly composed of bare soil. Tracks (8) and (9) are the only ones with a significant proportion of croplands, all in the intermediate NDVI strata. Tracks (2) and (6) are the only ones with a significant proportion of urban pixels, and are complemented with low to intermediate NDVI classes of low vegetation. Remaining tracks are a mix of forests with intermediate to high NDVI, and low vegetation with low to intermediate NDVI.

| | **bare** | **urban** | **crops** | | | **forests** | | | **low veg.** | | |
|---|---|---|---|---|---|---|---|---|---|---|---|
| **ndvi** | | | **low** | **inter** | **high** | **low** | **inter** | **high** | **low** | **inter** | **high** |
| (1) | **80.9** | 0.1 | 0.0 | 0.0 | 0.0 | 0.0 | 0.0 | 0.0 | **18.6** | 0.3 | 0.0 |
| (2) | 1.9 | **25.2** | 0.1 | 0.1 | 0.1 | 0.0 | 3.1 | 3.0 | **34.1** | **29.2** | 3.2 |
| (3) | **16.0** | 11.9 | 0.0 | 0.0 | 0.0 | 0.1 | **15.7** | 8.6 | **20.0** | **26.4** | 1.1 |
| (4) | 0.1 | 3.9 | 0.0 | 0.1 | 0.0 | 0.3 | **26.8** | **56.8** | 0.5 | 9.9 | 1.4 |
| (5) | **17.5** | 0.0 | 0.0 | 0.1 | 0.2 | 0.0 | 0.7 | 0.0 | **73.9** | 7.5 | 0.0 |
| (6) | 0.8 | **51.0** | 0.2 | 2.4 | 1.0 | 0.1 | 5.0 | 4.8 | 1.9 | **29.0** | 3.8 |
| (7) | 0.1 | 3.1 | 0.3 | 3.4 | 1.5 | 0.0 | **15.5** | **57.0** | 0.2 | 13.2 | 5.4 |
| (8) | 0.2 | 13.4 | 4.0 | **28.3** | 8.7 | 0.1 | 10.9 | 14.4 | 1.3 | **17.5** | 0.7 |
| (9) | 0.0 | 2.2 | 9.0 | **26.3** | 4.3 | 0.0 | 6.1 | 0.8 | **18.2** | **32.9** | 0.1 |
| (10) | 20.6 | 14.5 | 0.0 | 0.1 | 0.0 | 0.1 | 13.5 | 4.7 | **20.4** | **25.4** | 0.6 |
| (11) | 14.5 | 0.0 | 0.0 | 0.0 | 0.0 | 0.5 | **23.2** | 0.9 | **18.9** | **39.6** | 2.3 |
| (12) | 0.9 | 1.0 | 0.1 | 0.9 | 0.3 | 1.9 | **28.9** | **33.4** | 12.8 | 14.5 | 5.2 |

Table 5: Percentage of land-cover classes for each track. Vegetation classes are further stratified according to Landsat-8 NDVI into [0,0.2] (low), [0.2,0.6] (intermediate) and [0.6, 1.0] (high). Classes exceeding 15% of available pixels are highlighted in bold for the sake of readability.

## 3. Results

### *3.1. SBT difference analysis*

Table 6 shows the biases and RMSE of LST and SBT differences (Landsat-8 - MASTER), for each MASTER track, and for samples for which angles between viewing directions are below 7°. Though each track exhibits an absolute LST bias lower than 1.8 K (1.6 K for SBT), the biases of each track vary significantly within this range. Standard deviation values range from 0.7 K to up to 2.2 K for LST and 0.6K to 2K for SBT, if we exclude track (10) which exhibits a very large standard deviation. Those values are in line with recent Landsat-8 LST performance assessment for Landsat-8 Collection 2 Level 2 (Niclòs et al., 2021). For all tracks, SBT standard deviation is lower than LST standard deviation. SBT is therefore more suitable for the analysis in this paper, as it seems to discard discrepancies related to the different LST - emissivity separation methods detailed in section 2.2.2. In order to further reduce discrepancies unrelated to directional anisotropy, on each track SBT differences will be corrected from the bias, so that similar viewing angles between MASTER and Landsat-8 correspond to a null SBT difference on average. It is noteworthy that standard deviation in table 6 corresponds to the Root Mean Squared Error (RMSE) of the de-biased data.

Figure 4 shows the SBT difference maps for each track, which have been corrected from the biases shown in table 6. Most tracks exhibit a pattern related to the position in the MASTER swath, and thus to the MASTER VZA. This is for instance the case form tracks (2), (6), (7), (8) and (12), where MASTER SBT appears to be consistently warmer on the western side of the swath than on the eastern side of the swath. Tracks (4), (9) and (10) have the highest SBT difference standard deviations in table 6 and exhibit spatial patterns that seem uncorrelated to TIR anisotropy. Inspection of Landsat-8 cirrus band B9 in level 1C products from collection 2 reveals that track (10) is heavily contaminated by unmasked cirrus clouds, which explains both its high SBT difference standard deviation and large spatial patterns in SBT difference map. Likewise, a closer inspection of track (4) reveals that the SBT difference map is completely dominated by terrain effects, which explains both its high SBT difference standard-deviation and noisy spatial patterns. Inspection of remaining tracks reveals that track (9) is also partly

| | | LST | | SBT | |
|---|---|---|---|---|---|
| **Track** | **#samples** | **Bias** | **Std dev** | **Bias** | **Std dev** |
| (1) 2013-03-29 | 5187 | -0.6 | 0.7 | -0.7 | 0.6 |
| (2) 2013-04-11 | 69125 | 0.3 | 1.4 | 0.6 | 1.3 |
| (3) 2013-05-22 | 59011 | 1.4 | 1.6 | 1.1 | 1.5 |
| (4) 2013-12-05 | 7409 | 0.7 | 1.9 | 0.4 | 1.9 |
| (5) 2014-03-31 | 22037 | 1.2 | 1.0 | 0.9 | 0.6 |
| (6) 2014-04-14 | 73182 | 0.4 | 1.2 | 0.2 | 1.1 |
| (7) 2014-04-28 | 13012 | 0.6 | 1.0 | 1.0 | 1.0 |
| (8) 2014-06-06 | 138921 | -0.3 | 1.8 | -0.1 | 1.7 |
| (9) 2014-10-21 | 74247 | -1.5 | 2.1 | -1.5 | 2.1 |
| (10) 2015-05-28 | 97435 | -0.1 | 5.5 | -0.3 | 5.4 |
| (11) 2018-06-19 | 36706 | -1.3 | 1.7 | -1.6 | 1.6 |
| (12) 2021-03-30 | 62572 | -1.7 | 1.9 | -1.1 | 1.7 |

Table 6: Bias and RMSE of Land Surface Temperature and SBT difference (Landsat-8 - MASTER) for samples with an absolute viewing angles distance bellow 7°

contaminated by unmasked cirrus clouds and terrain effects. Tracks (4), (9) and (10) have therefore been excluded from the analysis in the remaining of this paper.

### *3.2. Directional effects analysis*

#### *3.2.1. Distance to hotspot vs. distance to Landsat-8 viewing direction*

In figure 5, SBT differences, corrected from the biases shown in table 6, are analysed with respect to both MASTER view angular distance to hotspot and to Landsat-8 viewing direction. All graphs exhibit the same v-shaped curve, which is induced by the relative viewing geometries between Landsat-8 and MASTER. Since Landsat-8 has a narrow FOV, the minimum angular distance between views occurs far from the hotspot condition (usually between 20° and 50° of distance to the hotspot), and with MASTER view close to Nadir. On the left of the minimum point, which corresponds to the western part of the MASTER swath, the MASTER view gets closer to the hotspot, which correlates with MASTER temperature getting hotter than Landsat-8 temperature. This is especially visible for tracks (2), (8) and (12), which are also the tracks that come closer to the hotspot. On the right of the minimum point, which corresponds to the eastern part of the MASTER swath, the view gets away from the hotspot condition, which correlates in most views with MASTER getting colder than Landsat-8. Tracks (1), (3), (5) and (11) will be further analysed in section 3.2.2.

#### *3.2.2. MASTER view zenith and azimuth*

Figure 6 allows to better understand the angular configurations of each MASTER track with respect to the position of the sun. Two kinds of configurations can be observed. In hotspot conditions, when the sun is close to the principal observation plane, as in tracks (2), (8) and (12), the temperature steadily increases while coming closer to the sun position. On track (8), MASTER view zenith gets higher than the sun zenith which results in a cool-down of the SBT. Track (12) shows that the sun is almost in the principal plane, which explains why this track has the smallest distance to the hotspot. When the sun is far from the principal observation plane however, SBT gets colder with higher view zenith angle, on both ends of the swath. The difference with Landsat-8 SBT comes to a minimum near nadir, but the position of this minimum varies and

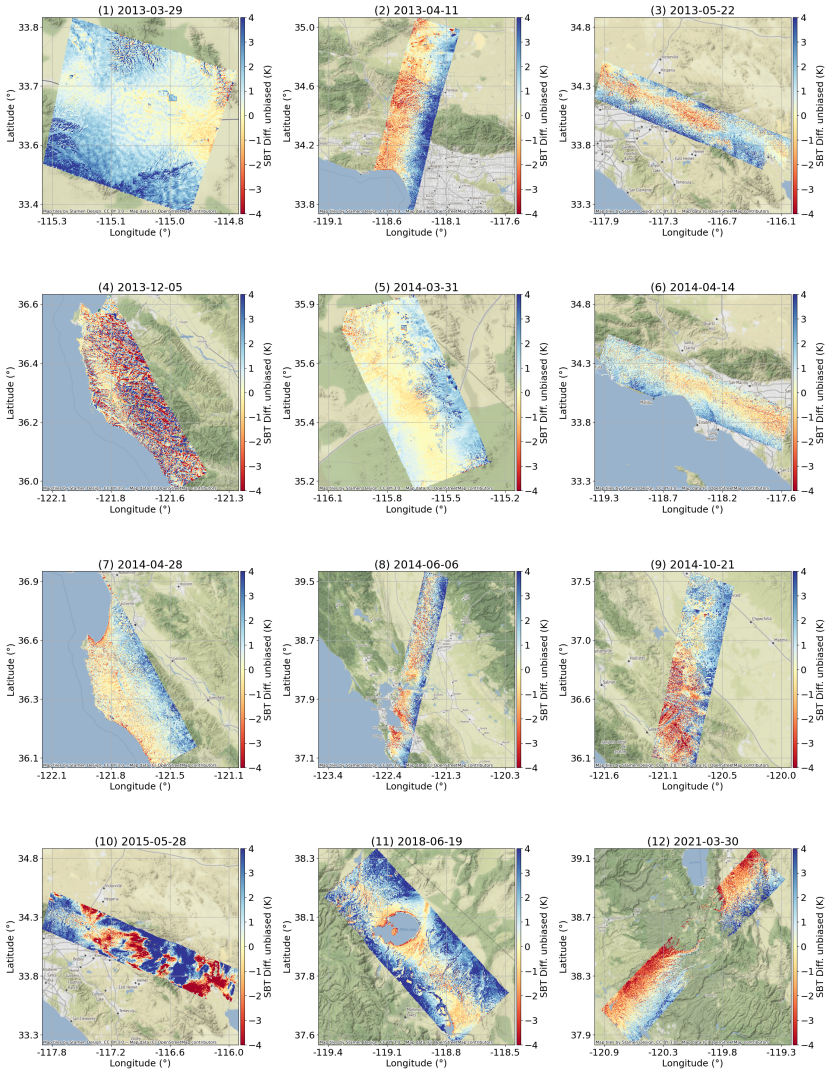


Figure 4: Maps of SBT difference (Landsat-8 - MASTER), corrected of the bias computed in table 6 for all tracks (negative values are in red and mean that MASTER is warmer than Landsat-8)

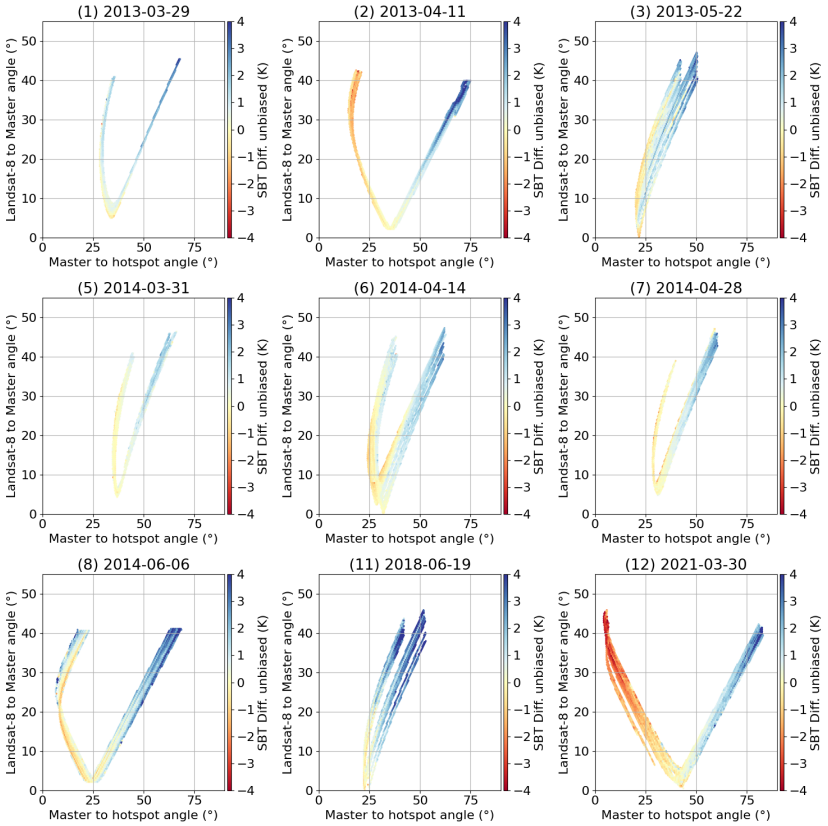


Figure 5: SBT difference (Landsat-8 - MASTER) with respect to angular distance from MASTER to hotspot and from MASTER to Landsat-8, corrected of the bias computed in table 6 (negative values are in red and mean that MASTER is warmer than Landsat-8)

seems to be influenced by the position of the sun. This may be related to gap fraction effect and can be observed on tracks (1), (3), (5), (6), (7) and (11).

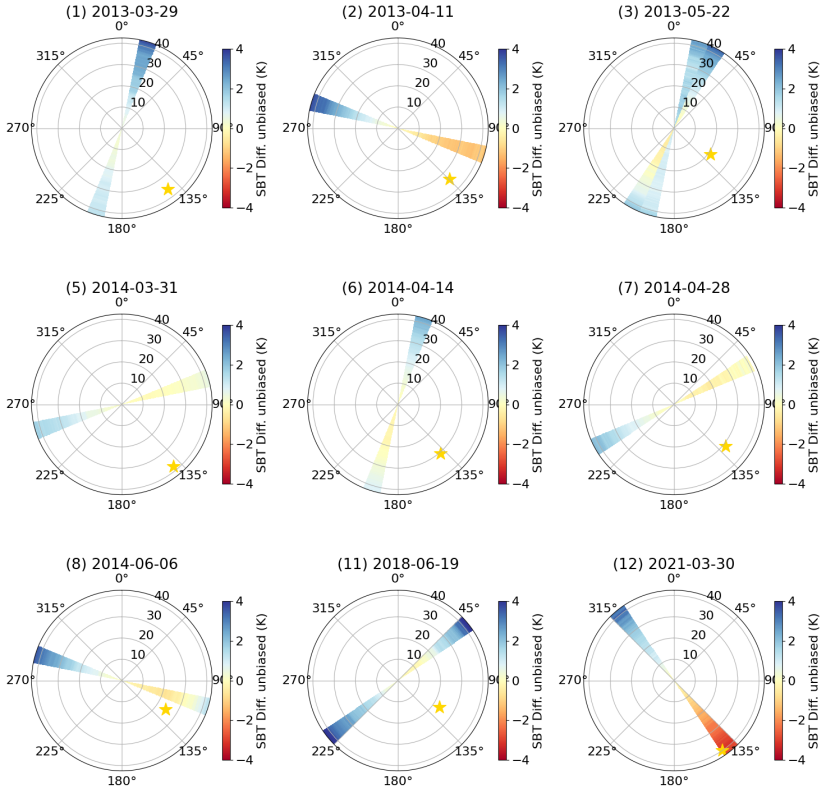


Figure 6: SBT difference (Landsat-8 - MASTER) with respect to MASTER view zenith and azimuth, corrected of the bias computed in table 6. Average sun position is marked by an orange star. (negative values are in red and mean that MASTER is warmer than Landsat-8)

Figure 7 allows better observing those two configurations. It shows the distributions of the bias-corrected SBT with respect to MASTER signed VZA (positive angle are to the east and therefore closer to the sun, negative to the west). The dotted red line indicates the mean difference, while the dashed red lines indicate ± 1 standard deviation. In configurations (2), (8) and (12) where the sun is almost in the principal plane and close to hotspot, MASTER SBT gets steadily warmer than Landsat-8 from east to west. For track (8), SBT starts to get colder past the sun zenith. For tracks (1), (3), (5), (6), (7) and (11), MASTER gets colder on both end of the swath, with a varying

position for the maximum position, which may be related to gap fraction. Dotted blue vertical lines indicate the FOV of the up-comping TRISHNA and SBG missions. One can note that the 1 standard deviation red dashed lines show that the standard deviation is almost constant throughout the MASTER signed VZA, and equal to standard deviation estimated in table 6. This standard deviation therefore probably accounts for uncertainties between sensors that are not related to TIR anisotropy.

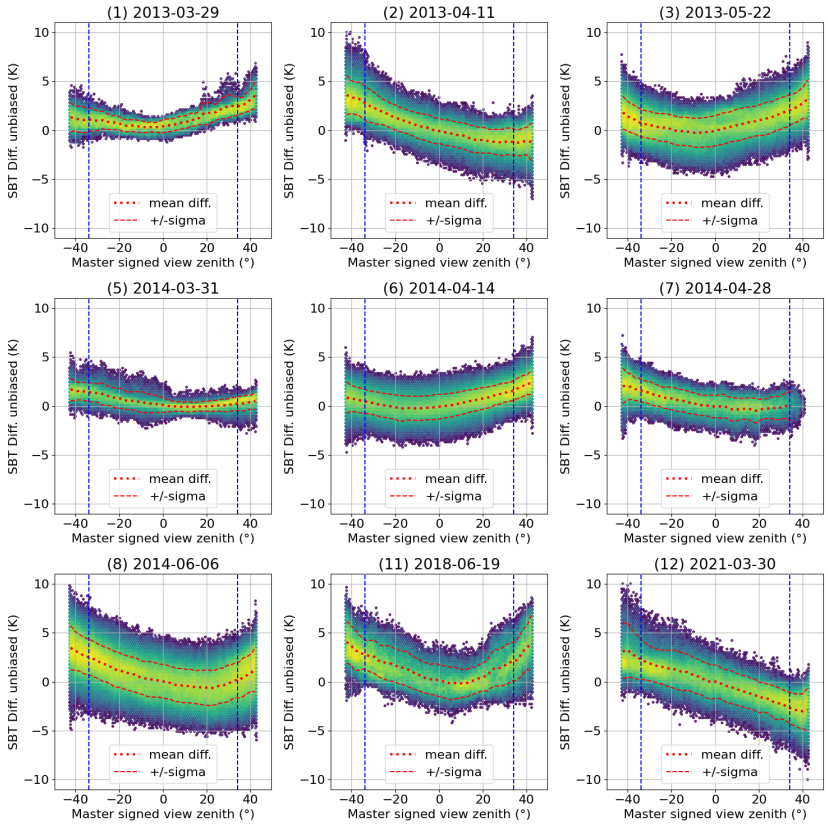


Figure 7: SBT difference, corrected of the bias computed in table 6, with respect to MASTER signed view zenith angle (positive angles are to the east, negative to the west). The solid red line indicates the mean values, the red dashed line indicates mean ± 1 standard deviation. Blue dotted lines indicate TRISHNA and SBG FOV.

Table 7 gives a quantitative analysis of the directional effects budget for each track, based on the mean difference trend for each track (see dotted red curves in figure 7).

Within MASTER FOV, the amplitude of directional effects ranges from 1.5K to more than 6K for track (12), the closest track to hotspot conditions. Restricted to the foreseen TRISHNA and SBG FOV, this budget value falls to 4.7K.

| | **MASTER** | | | | **Trishna** | | | |
|---|---|---|---|---|---|---|---|---|
| id | Min. | -43° | 43° | amp. | Min. | -34° | 34° | amp. |
| (1) 2013-03-29 | 0.3 | 1.3 | 3.6 | **3.3** | 0.3 | 1.1 | 2.5 | **2.2** |
| (2) 2013-04-11 | -1.3 | 3.6 | -1.2 | **4.9** | -1.2 | 2.6 | -1.2 | **3.9** |
| (3) 2013-05-22 | -0.3 | 1.8 | 3.2 | **3.4** | -0.3 | 0.7 | 1.9 | **2.2** |
| (5) 2014-03-31 | -0.1 | 1.7 | 0.5 | **1.8** | -0.1 | 1.4 | 0.2 | **1.5** |
| (6) 2014-04-14 | -0.3 | 0.8 | 2.4 | **2.7** | -0.3 | 0.4 | 1.5 | **1.7** |
| (7) 2014-04-28 | -0.5 | 2.0 | 0.1 | **2.5** | -0.5 | 1.5 | -0.0 | **2.0** |
| (8) 2014-06-06 | -0.7 | 3.5 | 1.2 | **4.1** | -0.7 | 2.5 | 0.1 | **3.1** |
| (11) 2018-06-19 | -0.2 | 4.1 | 4.0 | **4.3** | -0.2 | 2.7 | 2.0 | **2.9** |
| (12) 2021-03-30 | -3.0 | 3.1 | -2.9 | **6.3** | -2.4 | 2.2 | -2.5 | **4.7** |

Table 7: For each MASTER track, minimum average SBT difference, average SBT difference at both ends of swath and amplitude (amp.) of SBT difference between minimum and maximum are displayed, left for the MASTER FOV, right, for a limitation to TRISHNA FOV (all in K). The max-min column gives an estimate of directional effects.

### *3.2.3. Sensitivity to land-cover*

Figure 8 shows the mean and standard deviation curves of SBT difference with respect to MASTER signed view zenith angle, for the major land-cover classes (> 15%) highlighted in table 5. It can be observed that though slight differences may appear between classes on the same track, most of the time all classes follow a similar trend for a given track. The NDVI strata seems to be the main driver for consistency, as can be noted on track (1) and (5) with bare soil and low vegetation with low NDVI, on track (3) with forests and low vegetation, both with intermediate NDVI, and on track (8) between croplands and low vegetation, both with a low NDVI. On track (6), it can be observed that the urban class behaves very similarly to the low vegetation with low NDVI class, which may indicate that urban class in actually a fair mix of artificial and

vegetated surfaces. Track (3) might exhibit some sort of gap fraction effect, with intermediate NDVI classes getting to a lower minimum than low NDVI classes. Forests with high NDVI seem to behave slightly differently than other intermediate NDVI vegetation classes, with only two examples on track (7) and (12). Interestingly, forests with high NDVI also exhibit a smaller standard deviation with respect to other classes. Some kind of ordering can be observed for instance on track (7) and (11), with lower NDVI classes yielding lower differences.

It should however be noted that in most of the cases, mean curves of each classes are within the ± standard-deviation of other classes. This seems to indicate that in the 100 meter resolution range, with this combination of limited dataset and land-cover source, pixels are mixed and exhibit average directional trends rather than sharp vegetation or crop types related signatures. Due to the severe classes imbalance between tracks, estimating model parameters independently on each class would further reduce the variability of angular configurations and thus the significance of the experiment. A much larger dataset would be necessary for per-class estimation of models parameters. In the next section, model estimations will therefore only be performed jointly for all classes.

### *3.3. Directional model fitting*

#### *3.3.1. Per-track parameters estimation*

In this section, each of the five models presented in table 3 is fitted independently on de-biased SBT from each track, using the methodology presented in 2.3. Models are fitted using all pixels from all land-cover classes of a track, which provides the required variability to fit the 3 to 4 parameters depending on the model. Figure 9 shows how each model fits the scatter plot for each track. SBT differences are expressed as a percentage variation to facilitate the comparison with the model. All models seem to be able to fit the observed directional effects, with the RL and LSF-RL being slightly more versatile than the other, and the Vinnikov model struggling to cope with higher VZA. This can be observed for instance on tracks (2) and (12) where the Vinnikov model diverges below 0°. Hotspot shape seems to be correctly captured by the other four models in track (2), (8) and (12). Differences for all models start to show for

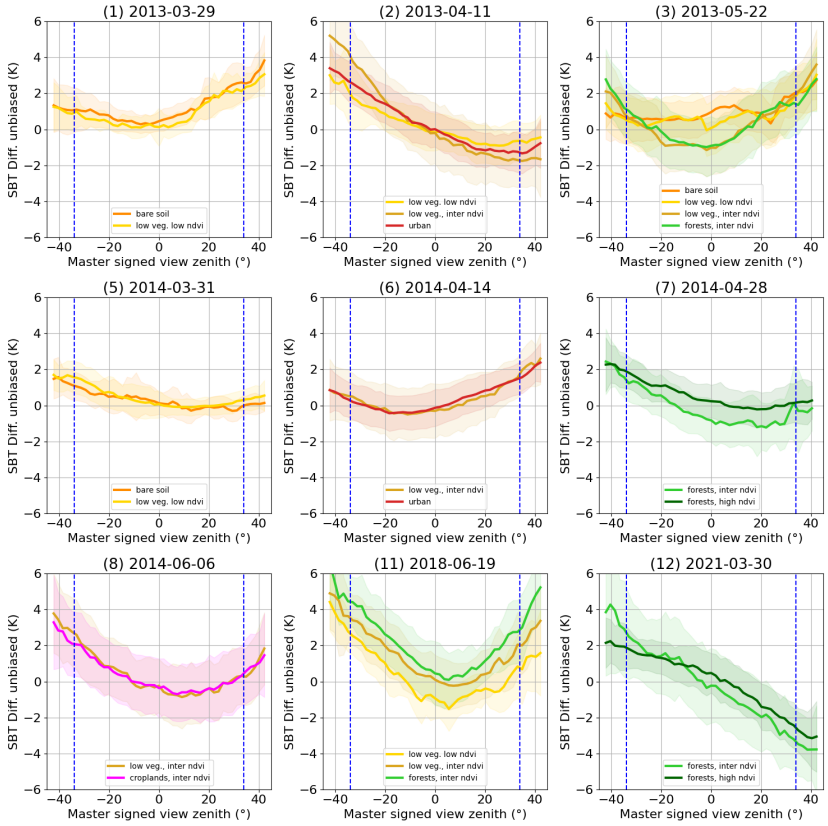


Figure 8: Mean ± standard-deviation of unbiased SBT difference with repect to MASTER signed view zenith angle for the major land-cover classes (> 15%) of each land cover classes as highlighted in table 5.

higher viewing angles close to or outside limits of the data range.

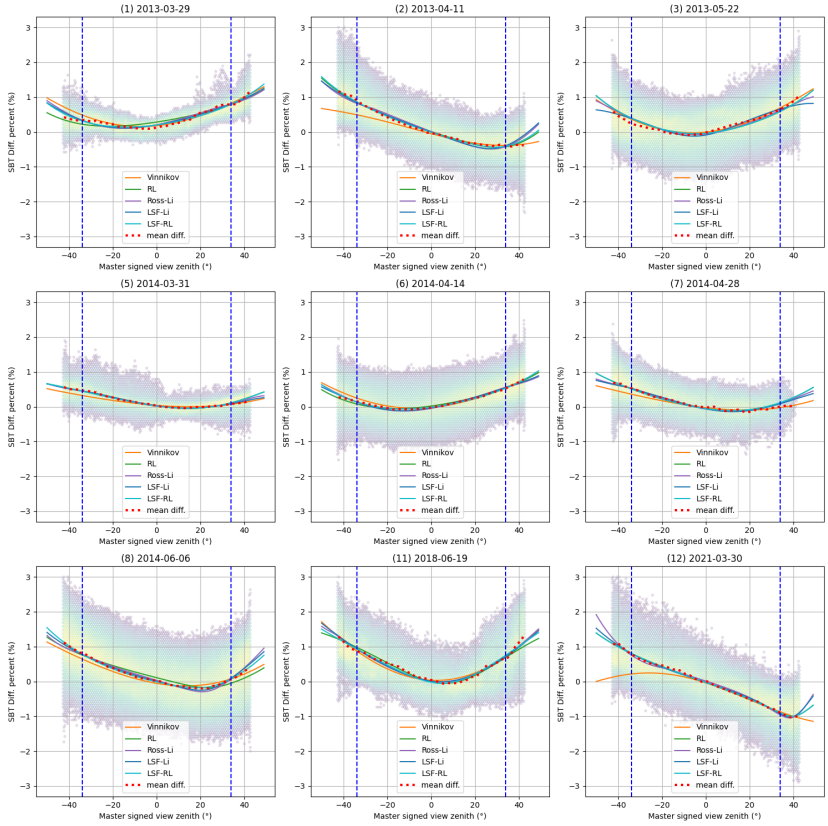


Figure 9: Least-Square fitting of the five TIR directional models from table 3 on SBT differences. Vertical axis represent the percentage of variation of SBT between Landsat-8 (considered as Nadir) and MASTER. In this figure, each model is fitted separately on each track.

In table 8, the correction performance of each model is measured for each track in terms of Root Mean Squared Error (RMSE) and amplitude (max - min of red curve in figure 7). Regarding RMSE, it can be observed that all models allow reducing the RMSE with respect to the uncorrected values. Though performances on RMSE improvement are very close from one model to another, the LSF-Li reaches the best performances for 8 tracks out of 9, while the Ross-Li and LSF-RL models reaches the best performances on 7 tracks out of 9. On track (12), which is the closest to the hotspot, all models seem to perform almost equally. Gains on RMSE range from 0.2K to 0.9K

depending on the track.

In Cao et al. (2019), lower RMSE are found on simulated data (bellow 0.5K). Thea authors recommend the following ranking for models (best to worst) : LSF-Li, Ross-Li, Vinnikov and RL. This is consistent with RMSE on table 8 with the LSF-Li being the best model 8 times out of 9, the Ross-Li, Vinnikov and LSF-RL models 7 times out of 9, and the RL model only 5 times out of 9.

In terms of directional effects amplitude, table 8 shows that all models allow to significantly reduce the amplitude, below 1 K for the majority of tracks. Reductions for tracks with high hotspot effects are particularly strong, with track (12) going from more than 6K to less than 0.7 K for instance. The Vinnikov model is the best model for more than half of the tracks, but tracks with strong hotspot effect such as (8) and (12) are won by either RL, LSF-Li or LSF-RL. Regarding amplitude, performances of the different models are less close to each others, but this can be explained by the use of maximum - minimum difference, which is highly sensitive to outliers. Gains on directional effects amplitude range from 1.6K to 5.8K depending on the track.

| **id** | **RMSE** | | | | | | **Amp** | | | | | |
|---|---|---|---|---|---|---|---|---|---|---|---|---|
| | **Raw** | **Vin.** | **RL** | **Ross** | **LSF** | **LRL** | **Raw** | **Vin.** | **RL** | **Ross** | **LSF** | **LRL** |
| (1) | 1.8 | **1.0** | **1.0** | **1.0** | **1.0** | **1.0** | 3.3 | **0.6** | 1.4 | 1.0 | 0.8 | 0.9 |
| (2) | 2.3 | **1.5** | **1.5** | **1.5** | **1.5** | **1.5** | 4.9 | **0.3** | 0.6 | 1.1 | 1.1 | 0.7 |
| (3) | 2.0 | **1.5** | 1.6 | 1.6 | **1.5** | 1.6 | 3.4 | **0.5** | 1.2 | 1.0 | 1.2 | 0.9 |
| (5) | 1.1 | **0.8** | **0.8** | **0.8** | **0.8** | **0.8** | 1.8 | 0.4 | 0.4 | 0.3 | **0.2** | 0.4 |
| (6) | 1.6 | **1.2** | **1.2** | **1.2** | **1.2** | **1.2** | 2.7 | **0.2** | 0.4 | 0.6 | 0.5 | 0.3 |
| (7) | 1.6 | **1.2** | **1.2** | **1.2** | **1.2** | **1.2** | 2.5 | **0.3** | 0.9 | 0.8 | 0.8 | 0.9 |
| (8) | 2.3 | **1.8** | 1.9 | **1.8** | **1.8** | **1.8** | 4.1 | 0.8 | 1.3 | 0.7 | 0.4 | **0.2** |
| (11) | 2.8 | 1.9 | 1.9 | 1.9 | 1.9 | **1.8** | 4.3 | 1.1 | 1.4 | **0.9** | 1.0 | 1.0 |
| (12) | 2.7 | 1.9 | 1.9 | **1.8** | **1.8** | 1.9 | 6.3 | 0.7 | **0.5** | 0.7 | **0.5** | **0.5** |

Table 8: Root Mean-Square error and amplitude (max - min of red curve in figure 7) for raw SBT corrected of the bias computed in table 6, and for MASTER temperature normalized with five models, with parameters estimated for each track. Note that model names have been shortened (Vin: Vinnikov, RL: Roujean-Lagouarde, Ross: Ross-Li, LSF: LSF-Li, LRL: LSF-RL).

Figure 10 shows the raw and corrected SBT with respect to the signed VZA for 5 tracks with very strong directional effects. It can be noted that the correction does not seem to have any effect on the standard-deviation, and thus it does not amplify or create any noise. For track (2), the best model in terms of amplitude is Vinnikov according to table 8, closely followed by RL and LSF, though it can be observed that the Ross-Li and LSF-Li models struggle at higher VZA (out of TRISHNA FOV). For track (3), the best model is also Vinnikov, with amplitude two times less than the next best model, which is RL. Indeed, the latter seems to fail to completely compensate the directional trends, with SBT differences still slightly positives for positive VZA and negative for negative VZA. On track (8), the best model is LSF-RL by a large amount according to table 8, which is confirmed on figure 10 with a smooth a regular corrected SBT.

Although directional trends are considerably reduced after correction, there are remaining trends in almost all models, and all of them struggle at higher VZA. Track (11) is noisier and the model fitting is poorer, with only the Ross-Li model achieving a correction with an amplitude below 1 K, though differences on figure 10 are not obvious. For track (12), which is the track with the strongest hotspot effect due to the proximity of MASTER viewing direction and solar direction (see figure 6), LSF-Li, RL and LSF-RL models have the best performances according to table 8 which is confirmed on figure 10 by fewer oscillations for higher VZA.

### *3.3.2. Global models parameters estimation*

Fitting models on each track separately allows to assess how well those models explain the observed data. However, this strategy does not apply to operational directional corrections in ground segments, where simultaneous observations will not be available to fit the models. This section investigates the performances of global models, with a single set of parameters for each model to correct all tracks at once. Parameters of those global models are fitted on all pixels from all tracks altogether, using the methodology presented in 2.3. Figure 11 shows how well those global models fit the scatter plots for each track. It can be observed that even if the goodness of fit is lesser than in figure 9, it is still relatively high. However, global models also struggle to model the near hotspot conditions of track (12).

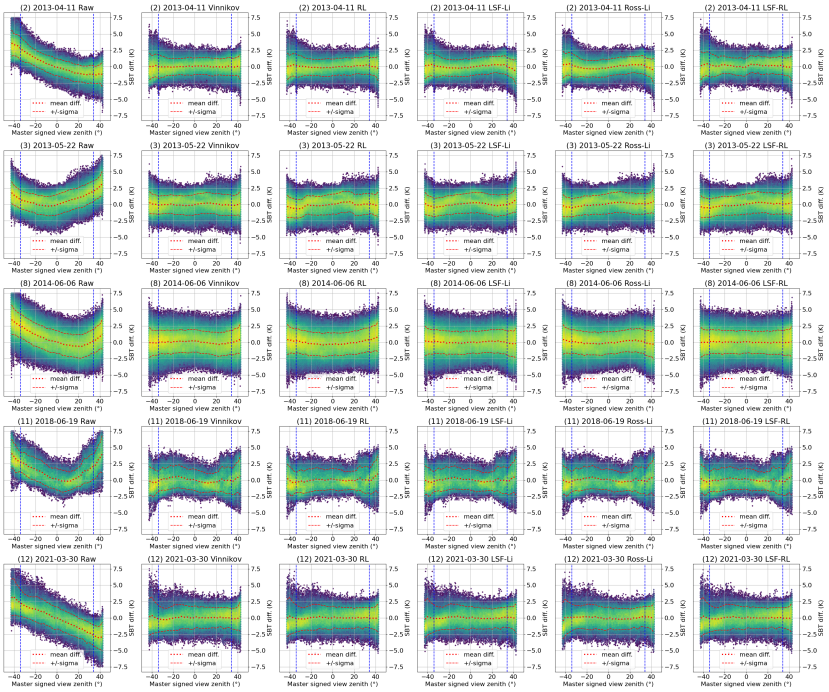


Figure 10: Corrected SBT versus signed VZA for raw and model-corrected SBT, for 5 tracks with high directional effects amplitudes. Blue dashed lines indicate Trishna FOV.

Table 9 shows the quantitative performance analysis of global models. As in table 8, no model clearly outperform the others. All models achieve a systematic decrease of RMSE ranging from 0.2K to 0.9K and a systematic decrease of directional effects amplitude ranging from 1.3K to 4.8K. Even if their performances are lower than those achieved by per track models presented in section 3.3.1, global models still provide valuable corrections. It can be observed that if the RL model is frequently the best model in terms of RMSE, it is never the best model in terms of amplitude. The ranking according to the number of times a model is the best model in terms of RMSE is the following (best to worst) : RL, LSF-RL, Vinnikov and LSF-Li, Ross-Li. This ranking differs from the ranking of Cao et al. (2019), in which models are not fitted globally.

| **id** | **RMSE** | | | | | | **Amp** | | | | | |
|---|---|---|---|---|---|---|---|---|---|---|---|---|
| | **Raw** | **Vin.** | **RL** | **Ross** | **LSF** | **LRL** | **Raw** | **Vin.** | **RL** | **Ross** | **LSF** | **LRL** |
| (1) | 1.8 | 1.2 | 1.3 | **1.0** | **1.0** | 1.2 | 3.3 | 1.2 | 1.2 | 1.6 | **0.9** | 1.0 |
| (2) | 2.3 | **1.5** | 1.6 | 1.6 | 1.6 | 1.6 | 4.9 | **1.0** | 1.8 | 1.8 | 2.2 | 2.0 |
| (3) | 2.0 | **1.6** | **1.6** | **1.6** | **1.6** | **1.6** | 3.4 | **1.2** | 1.3 | 1.4 | **1.2** | 1.4 |
| (5) | 1.1 | 0.9 | **0.8** | 1.2 | 1.1 | **0.8** | 1.8 | 1.1 | 0.6 | **0.5** | 1.1 | 0.7 |
| (6) | 1.6 | **1.2** | **1.2** | **1.2** | **1.2** | **1.2** | 2.7 | 0.6 | 0.5 | 0.7 | 0.7 | **0.3** |
| (7) | 1.6 | **1.2** | **1.2** | 1.3 | 1.3 | **1.2** | 2.5 | **0.8** | 0.9 | 1.0 | 1.4 | 1.0 |
| (8) | 2.3 | **1.9** | **1.9** | 2.0 | **1.9** | **1.9** | 4.1 | 1.4 | 1.9 | 1.9 | **1.0** | 1.4 |
| (11) | 2.8 | 2.2 | **1.9** | 2.2 | 2.1 | **1.9** | 4.3 | 2.8 | 2.1 | 2.8 | **1.9** | **1.9** |
| (12) | 2.7 | 2.1 | **2.0** | 2.1 | **2.0** | 2.1 | 6.3 | 2.5 | 2.7 | 1.7 | **1.5** | 3.2 |

Table 9: Root Mean-Square error and amplitude (max - min of red curve in figure 7) for raw SBT corrected of the bias computed in table 6, and for MASTER temperature normalized with five models, with parameters jointly estimated on all tracks.Note that model names have been shortened (Vin: Vinnikov, RL: Roujean-Lagouarde, Ross: Ross-Li, LSF: LSF-Li, LRL: LSF-RL).

Figure 12 presents the same tracks as in figure 10 but corrected with the global models. While all tracks exhibit residual angular trends, within the TRISHNA FOV, all models exhibit performances that may be of interest for downstream applications. Track (11) has the highest residual effects, which is compliant with figures in table 9,

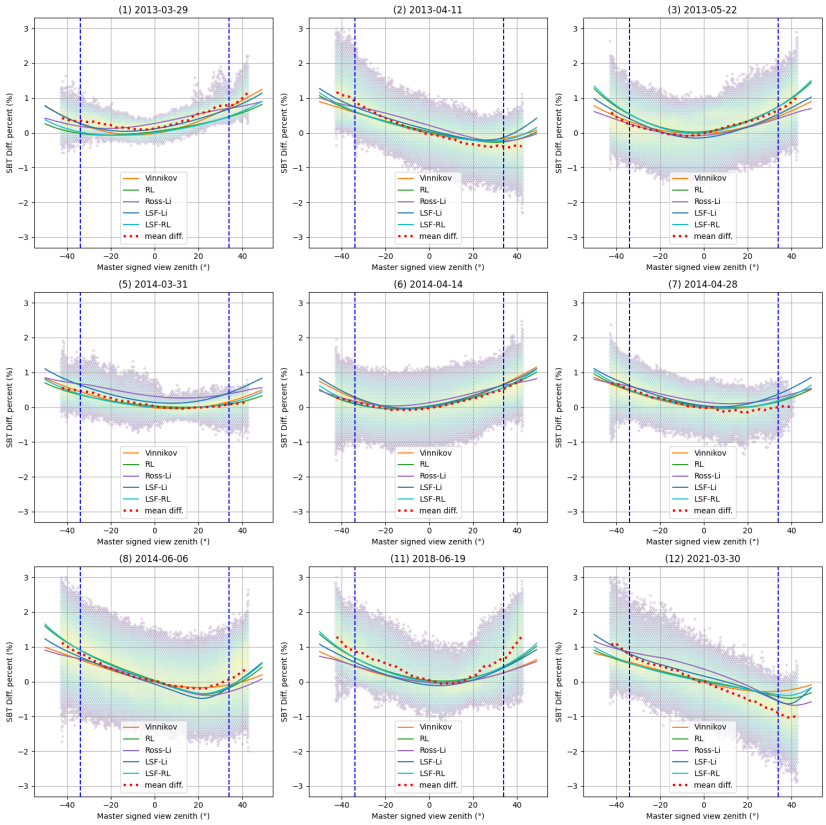


Figure 11: Least-Square fitting of the five TIR directional models from table 3 on SBT differences. Vertical axis represent the percentage of variation of SBT between Landsat-8 (considered as Nadir) and MASTER. In this figure, each model is jointly fitted on all tracks.

showing a residual amplitude of around 2K for all models. On track (12), which is the closest to hotspot conditions, the Vinnikov and LSF-RL model perform poorly with respect to the other models, the former even introduces an artificial angular trend while the latter fails to completely capture the angular tend. All remaining models on track (12) significantly reduce the angular trend that can be observed in raw SBT differences.

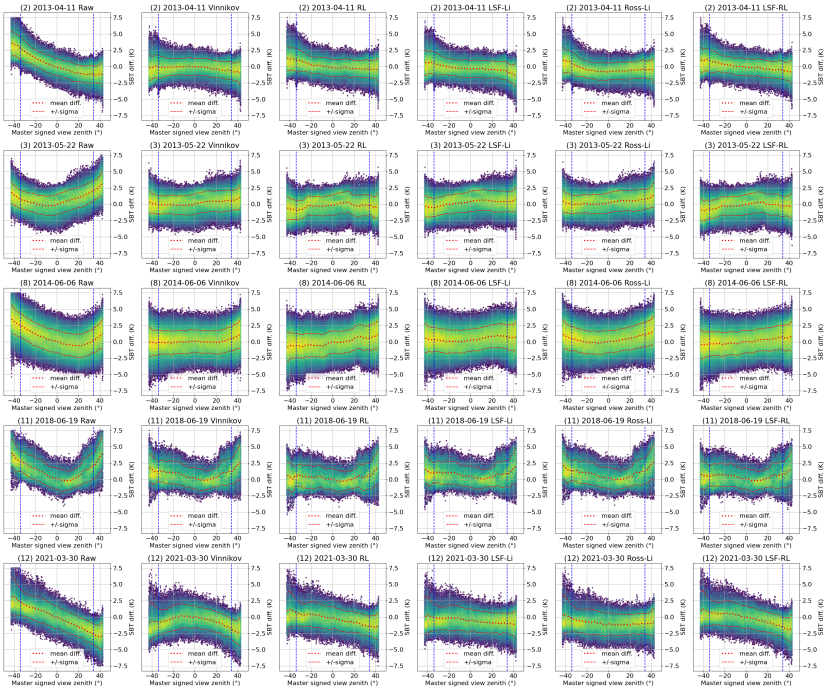


Figure 12: Corrected SBT versus signed VZA for raw and model-corrected SBT, using models jointly fitted on all tracks, for 5 tracks with high directional effects amplitudes. Blue dashed lines indicate TRISHNAp FOV.

Figure 13 presents a complete viewing angles sampling of each global model, in the mean solar conditions of track (12). All models seem to have captured the hotspot effect, while the shape of the hotspot itself varies from one model to another. the Vinnikov model hotspot seems ahead of the sun zenith angle, which may explain its lesser performance in correcting track (12). Table 10 shows the estimated parameters for each model. One can note that the Ross-Li Volumetric kernel contribution is very low with respect to the others.

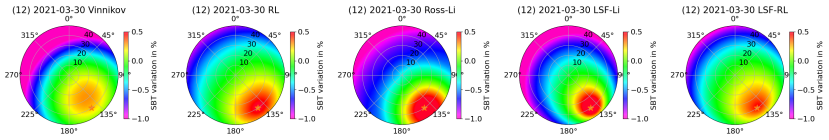


Figure 13: Polar plot of the different models, jointly fitted on all tracks, using average solar angles of track (12). Sun position is indicated by an orange star mark.

| **Model** | $k_0$ | $k_1$ | $k_2$ | $k_{hs}$ |
|---|---|---|---|---|
| Ross-Li | 1 | -7.4e-16 | 0.0091 | |
| LSF-Li | 1.2 | -0.22 | 0.011 | |
| Vinnikov | 1 | -0.023 | 0.024 | |
| RL | 1 | | 0.0061 | 1.8e-07 |
| LSF-RL | 1 | -0.047 | 0.0058 | 9.7e-07 |

Table 10: Parameters of the global models, estimated from all pairs

## 4. Discussion

This study exhibits evidences of strong directional effects up to an amplitude of 6K within a FOV of ± 45°, with real high-resolution TIR data, and shows encouraging performances of state-of-the art parametric models to mitigate their impact on temperature accuracy. However, two aspects of this work need to be further analysed and discussed: the inherent limitations related to the scarce data availability on one hand, and the derivation of the model parameters in a real-world ground segment scenario.

### *4.1. Limitations of the study*

Due to the scarce availability of simultaneous observations between MASTER and Landsat-8 on one hand, and the limited coverage of MASTER flights on the other, this study only covers a limited range of landscapes, all of them located in California, USA. Therefore, it can not be used to draw solid conclusions on other kinds of landscapes such as desert bare soil, very dense rain-forest canopy or tundras for instance. The geographic limitations also come with a low variety of solar angle conditions, excluding extreme latitudes and equator for instance.

Moreover, since this study relies on Landsat-8 acquisitions which have a local over-passing time of approximately 10:30 AM, its results are mainly valid for medium morning sun angles, whereas most upcoming missions will have a local over-passing time around noon. The solar zenith angle will therefore be lower, leading to solar angular conditions that have not been analysed in this study. As hotspot conditions will be more frequent, It is conjectured to observe lower but more frequent directional effects for sun position closer to zenith, but in the mean time SBT values could be higher.

Finally, this study adopts an undiscriminating point of view regarding the actual land-cover of each pixel, whereas the literature, which is driven by work on radiative transfer modeling, strongly suggests that different models or at least model parameters should be applied to different land-covers. We analysed the influence of land-cover on TIR anisotropy in section 3.2.3. We observed that classes seem to be mixed in our 100 meter resolution dataset, and exhibit similar angular trends. The land-cover agnostic approach was therefore privileged. However, this could be revisited if a larger dataset was to be acquired, with more landscape variability. It must be stressed that if a directional effect correction is to be implemented into up-coming missions ground-segment as a routine level 2 processing, relying on land-cover discrimination and phenology will be hard to achieve for a global coverage mission. Nevertheless, exogenous land-cover and phenology maps could be used for that purpose (Phiri et al., 2020). Last, TIR directional effects in urban environment follow very different physical causes and trends (Lagouarde and Irvine, 2008; Lagouarde et al., 2010), and may require different models, such as the combinations of base kernels investigated in Jiang et al. (2021).

### *4.2. Model parameters estimation for up-coming ground segments*

Another open question is whether such a correction is to be implemented within future ground segments and which credit to give to the estimated model parameters over time. In this study, models have first been fitted to each track independently, resulting in good correction performances of up to 5.8K in amplitude, but with important variations of the parameters from one track to another. Such variability suggests that model parameters might depend on the canopy structure as well as on the observation conditions they are fitted to. For instance, the RL kernel, is the best performing kernel

for track (12) that is closest to hotspot condition, which can be explained either because this model is a good model for hotspot or because it requires hotspot condition to be fitted properly. It must however again be stressed that such scene based individual parameters estimation is out of reach for routinely correcting data from global coverage satellites such as TRISHNA, LSTM or SBG.

On the other hand, the global models that have been fitted simultaneously on all tracks still exhibit interesting correction performances of up to 4.7K in the studied tracks. This work therefore suggests that such global models could be used routinely in a ground segment and be beneficial for downstream applications, with the limitations already highlighted in section 4.1.

While the determination of factors that should drive model parameters is probably best served by the physical process modelling scientific community, this paper proposes valuable dataset and methodology to assess model performances before putting them into production. Though in this work the analysed data are limited to 9 tracks in California, in the future, MASTER or other airborne TIR sensors with wide FOVs might be used to acquire more of those simultaneous observations with the Landsat series, effectively building a database for the assessment and calibration of directional parametric models, should attention be paid to the simultaneous over-passing time.

## 5. Conclusion

In this paper, simultaneous observations in space and time between Landsat-8 and the wide FOV MASTER airborne TIR sensors have been leveraged to analyse potential directional effects and their error budget for up-coming High Resolution TIR missions. Nine MASTER tracks where identified with a Landsat-8 overpass during the flight and the analysis of their SBT differences exhibits directional effects ranging from 1.6K to more than 6K within MASTER full FOV depending to the proximity to hotspot conditions. Three tracks are close to those conditions and one is almost within the principal acquisition plane, leading to the highest 6K amplitude. Other tracks also exhibit evidences of the gap fraction effect. Five state-of-the-art parametric models for TIR anisotropy have been selected from the literature for having been extensively tested on

simulated data. Those five models have been fitted to each of the identified MASTER track, using Landsat-8 as the target Nadir SBT of reference. The corrected temperature exhibits a systematic decrease of the RMSE of 0.2K to 0.9K, and a reduction of the amplitude associated to directional effects of 1.6K to 5.8K, bringing down the directional error budget to less that 1K in almost all cases. Global models, fitted simultaneously on all valid tracks, have also been assessed, with a reduction of RMSE of 0.2K to 0.8K and a reduction of the directional effect amplitude of 1.3K to 4.7K, bringing down the directional error budget below 2K in most cases. Those results suggest that future ground segments of up-coming high-resolution missions with a FOV greater than 30° would benefit from implementing such a correction. While in theory the LSF-RL model is the most suited to account for both the gap fraction and hotspot effects observed in figure 6, the LSF-RL model does not significantly outperform the other models in this study, which may be due to the limited amount of data, especially for the fitting of its extra parameter. This paper also lays grounds for a directional model in flight calibration procedure for those up-coming missions, should more airborne data be gathered during Landsat overpasses in the future.

The data used in this study have been made publicly available as an open dataset (Michel et al., 2023).

## References


M. Anderson, J. Norman, W. Kustas, R. Houborg, P. Starks, N. Agam, A thermal-based remote sensing technique for routine mapping of land-surface carbon, water and energy fluxes from field to regional scales, Remote Sensing of Environment 112 (2008) 4227–4241. URL: https://www.sciencedirect.com/science/article/pii/S0034425708002289. doi:https://doi.org/10.1016/j.rse.2008.07.009.

J. C. Price, Estimation of Regional Scale Evapotranspiration Through Analysis of Satellite Thermal-infrared Data, IEEE Transactions on Geoscience and Remote Sensing GE-20 (1982) 286–292. doi:10.1109/TGRS.1982.350445, conference Name: IEEE Transactions on Geoscience and Remote Sensing.

D. Courault, B. Seguin, A. Olioso, Review on estimation of evapotranspiration from remote sensing data: From empirical to numerical modeling approaches, Irrigation and Drainage Systems 19 (2005) 223–249. URL: https://doi.org/10.1007/s10795-005-5186-0. doi:10.1007/s10795-005-5186-0.

M. C. Anderson, R. G. Allen, A. Morse, W. P. Kustas, Use of Landsat thermal imagery in monitoring evapotranspiration and managing water resources, Remote Sensing of Environment 122 (2012) 50–65. URL: https://www.sciencedirect.com/science/article/pii/S0034425712000326. doi:10.1016/j.rse.2011.08.025.

G. Boulet, B. Mougenot, J.-P. Lhomme, P. Fanise, Z. Lili-Chabaane, A. Olioso, M. Bahir, V. Rivalland, L. Jarlan, O. Merlin, B. Coudert, S. Er-Raki, J.-P. Lagouarde, The SPARSE model for the prediction of water stress and evapotranspiration components from thermal infra-red data and its evaluation over irrigated and rainfed wheat, Hydrology and Earth System Sciences 19 (2015) 4653–4672. URL: https://hess.copernicus.org/articles/19/4653/2015/. doi:10.5194/hess-19-4653-2015, publisher: Copernicus GmbH.

R. Ishimwe, K. Abutaleb, F. Ahmed, et al., Applications of thermal imaging in agriculture—a review, Advances in remote Sensing 3 (2014) 128.

J.-P. Lagouarde, B. Bhattacharya, P. Crébassol, P. Gamet, S. S. Babu, G. Boulet, X. Briottet, K. Buddhiraju, S. Cherchali, I. Dadou, G. Dedieu, M. Gouhier, O. Hagolle, M. Irvine, F. Jacob, A. Kumar, K. K. Kumar, B. Laignel, K. Mallick, C. Murthy, A. Olioso, C. Ottlé, M. R. Pandya, P. V. Raju, J.-L. Roujean, M. Sekhar, M. V. Shukla, S. K. Singh, J. Sobrino, R. Ramakrishnan, The Indian-French Trishna Mission: Earth Observation in the Thermal Infrared with High Spatio-Temporal Resolution, in: IGARSS 2018 - 2018 IEEE International Geoscience and Remote Sensing Symposium, 2018, pp. 4078–4081. doi:10.1109/IGARSS.2018.8518720, iSSN: 2153-7003.

K. Cawse-Nicholson, P. A. Townsend, D. Schimel, A. M. Assiri, P. L. Blake, M. F. Buongiorno, P. Campbell, N. Carmon, K. A. Casey, R. E. Correa-Pabón, K. M.

Dahlin, H. Dashti, P. E. Dennison, H. Dierssen, A. Erickson, J. B. Fisher, R. Frouin, C. K. Gatebe, H. Gholizadeh, M. Gierach, N. F. Glenn, J. A. Goodman, D. M. Griffith, L. Guild, C. R. Hakkenberg, E. J. Hochberg, T. R. H. Holmes, C. Hu, G. Hulley, K. F. Huemmrich, R. M. Kudela, R. F. Kokaly, C. M. Lee, R. Martin, C. E. Miller, W. J. Moses, F. E. Muller-Karger, J. D. Ortiz, D. B. Otis, N. Pahlevan, T. H. Painter, R. Pavlick, B. Poulter, Y. Qi, V. J. Realmuto, D. Roberts, M. E. Schaepman, F. D. Schneider, F. M. Schwandner, S. P. Serbin, A. N. Shiklomanov, E. N. Stavros, D. R. Thompson, J. L. Torres-Perez, K. R. Turpie, M. Tzortziou, S. Ustin, Q. Yu, Y. Yusup, Q. Zhang, NASA's surface biology and geology designated observable: A perspective on surface imaging algorithms, Remote Sensing of Environment 257 (2021) 112349. URL: https://www.sciencedirect.com/science/article/pii/S0034425721000675. doi:10.1016/j.rse.2021.112349.

B. Koetz, W. Bastiaanssen, M. Berger, P. Defourney, U. Del Bello, M. Drusch, M. Drinkwater, R. Duca, V. Fernandez, D. Ghent, R. Guzinski, J. Hoogeveen, S. Hook, J.-P. Lagouarde, G. Lemoine, I. Manolis, P. Martimort, J. Masek, M. Massart, C. Notarnicola, J. Sobrino, T. Udelhoven, High Spatio- Temporal Resolution Land Surface Temperature Mission - a Copernicus Candidate Mission in Support of Agricultural Monitoring, in: IGARSS 2018 - 2018 IEEE International Geoscience and Remote Sensing Symposium, 2018, pp. 8160–8162. doi:10.1109/IGARSS.2018.8517433, iSSN: 2153-7003.

S. Mwangi, G. Boulet, A. Olioso, Assessment of an extended sparse model for estimating evapotranspiration from directional thermal infrared data, Agricultural and Forest Meteorology 317 (2022) 108882. URL: http://dx.doi.org/10.1016/j.agrformet.2022.108882. doi:10.1016/j.agrformet.2022.108882.

Z.-L. Li, B.-H. Tang, H. Wu, H. Ren, G. Yan, Z. Wan, I. F. Trigo, J. A. Sobrino, Satellite-derived land surface temperature: Current status and perspectives, Remote Sensing of Environment 131 (2013) 14–37. URL: http://dx.doi.org/10.1016/j.rse.2012.12.008. doi:10.1016/j.rse.2012.12.008.

D. L. Jupp, A. H. Strahler, A hotspot model for leaf canopies, Remote Sensing of Environment 38 (1991) 193–210.

T. Nilson, Inversion of gap frequency data in forest stands, Agricultural and Forest Meteorology 98-99 (1999) 437–448. URL: http://dx.doi.org/10.1016/S0168-1923(99)00114-8. doi:10.1016/s0168-1923(99)00114-8.

B. Cao, J.-L. Roujean, J.-P. Gastellu-Etchegorry, Q. Liu, Y. Du, J.-P. Lagouarde, H. Huang, H. Li, Z. Bian, T. Hu, B. Qin, X. Ran, Q. Xiao, A general framework of kernel-driven modeling in the thermal infrared domain, Remote Sensing of Environment 252 (2021) 112157. URL: http://dx.doi.org/10.1016/j.rse.2020.112157. doi:10.1016/j.rse.2020.112157.

J.-P. Lagouarde, S. Dayau, P. Moreau, D. Guyon, Directional anisotropy of brightness surface temperature over vineyards: Case study over the medoc region (sw france), IEEE Geoscience and Remote Sensing Letters 11 (2014) 574–578. doi:10.1109/LGRS.2013.2282492.

J. A. Sobrino, J. Cuenca, Angular variation of thermal infrared emissivity for some natural surfaces from experimental measurements, Applied Optics 38 (1999) 3931. URL: http://dx.doi.org/10.1364/ao.38.003931. doi:10.1364/ao.38.003931.

S. L. Ermida, I. F. Trigo, G. Hulley, C. C. DaCamara, A multi-sensor approach to retrieve emissivity angular dependence over desert regions, Remote Sensing of Environment 237 (2020) 111559. URL: http://dx.doi.org/10.1016/j.rse.2019.111559. doi:10.1016/j.rse.2019.111559.

J.-L. Roujean, M. Leroy, P.-Y. Deschamps, A bidirectional reflectance model of the earth's surface for the correction of remote sensing data, Journal of Geophysical Research 97 (1992) 20455. URL: http://dx.doi.org/10.1029/92jd01411. doi:10.1029/92jd01411.

W. Wanner, X. Li, A. H. Strahler, On the derivation of kernels for kernel-driven models

of bidirectional reflectance, Journal of Geophysical Research 100 (1995) 21077. URL: http://dx.doi.org/10.1029/95jd02371. doi:10.1029/95jd02371.

J.-L. Roujean, A parametric hot spot model for optical remote sensing applications, Remote Sensing of Environment 71 (2000) 197–206. URL: http://dx.doi.org/10.1016/s0034-4257(99)00080-2. doi:10.1016/s0034-4257(99)00080-2.

M. Claverie, J. Ju, J. G. Masek, J. L. Dungan, E. F. Vermote, J.-C. Roger, S. V. Skakun, C. Justice, The harmonized landsat and sentinel-2 surface reflectance data set, Remote Sensing of Environment 219 (2018) 145 – 161. doi:https://doi.org/10.1016/j.rse.2018.09.002.

C. Duffour, J.-P. Lagouarde, A. Olioso, J. Demarty, J.-L. Roujean, Driving factors of the directional variability of thermal infrared signal in temperate regions, Remote Sensing of Environment 177 (2016) 248–264.

B. Cao, Q. Liu, Y. Du, J.-L. Roujean, J.-P. Gastellu-Etchegorry, I. F. Trigo, W. Zhan, Y. Yu, J. Cheng, F. Jacob, et al., A review of earth surface thermal radiation directionality observing and modeling: Historical development, current status and perspectives, Remote Sensing of Environment 232 (2019) 111304.

Z. Bian, J.-L. Roujean, J.-P. Lagouarde, B. Cao, H. Li, Y. Du, Q. Liu, Q. Xiao, Q. Liu, A semi-empirical approach for modeling the vegetation thermal infrared directional anisotropy of canopies based on using vegetation indices, ISPRS Journal of Photogrammetry and Remote Sensing 160 (2020) 136–148. URL: http://dx.doi.org/10.1016/j.isprsjprs.2019.12.004. doi:10.1016/j.isprsjprs.2019.12.004.

Z. Bian, J. Roujean, T. Fan, Y. Dong, T. Hu, B. Cao, H. Li, Y. Du, Q. Xiao, Q. Liu, An angular normalization method for temperature vegetation dryness index (tvdi) in monitoring agricultural drought, Remote Sensing of Environment 284 (2023) 113330. URL: http://dx.doi.org/10.1016/j.rse.2022.113330. doi:10.1016/j.rse.2022.113330.

712 P. Yang, E. Prikaziuk, W. Verhoef, C. van der Tol, Scope 2.0: a model to simulate veg-
713 etated land surface fluxes and satellite signals, Geoscientific Model Development 14
714 (2021) 4697–4712. URL: http://dx.doi.org/10.5194/gmd-14-4697-2021.
715 doi:10.5194/gmd-14-4697-2021.

716 J. Gastellu-Etchegorry, Modeling radiative transfer in heterogeneous 3-d veg-
717 etation canopies, Remote Sensing of Environment 58 (1996) 131–156.
718 URL: http://dx.doi.org/10.1016/0034-4257(95)00253-7. doi:10.1016/
719 0034-4257(95)00253-7.

720 J.-P. Gastellu-Etchegorry, N. Lauret, T. Yin, L. Landier, A. Kallel, Z. Malenovsky,
721 A. A. Bitar, J. Aval, S. Benhmida, J. Qi, G. Medjdoub, J. Guilleux, E. Chavanon,
722 B. Cook, D. Morton, N. Chrysoulakis, Z. Mitraka, Dart: Recent advances in remote
723 sensing data modeling with atmosphere, polarization, and chlorophyll fluorescence,
724 IEEE Journal of Selected Topics in Applied Earth Observations and Remote Sens-
725 ing 10 (2017) 2640–2649. URL: http://dx.doi.org/10.1109/jstars.2017.
726 2685528. doi:10.1109/jstars.2017.2685528.

727 S. L. Ermida, I. F. Trigo, C. C. DaCamara, J.-L. Roujean, Assessing
728 the potential of parametric models to correct directional effects on local to
729 global remotely sensed LST, Remote Sensing of Environment 209 (2018)
730 410–422. URL: https://www.sciencedirect.com/science/article/pii/
731 S0034425718300798. doi:10.1016/j.rse.2018.02.066.

732 A. Pinheiro, J. Privette, P. Guillevic, Modeling the observed angular anisotropy of
733 land surface temperature in a savanna, IEEE Transactions on Geoscience and Re-
734 mote Sensing 44 (2006) 1036–1047. URL: http://dx.doi.org/10.1109/tgrs.
735 2005.863827. doi:10.1109/tgrs.2005.863827.

736 Z. Bian, B. Cao, H. Li, Y. Du, J.-P. Lagouarde, Q. Xiao, Q. Liu, An analytical four-
737 component directional brightness temperature model for crop and forest canopies,
738 Remote Sensing of Environment 209 (2018) 731–746. URL: http://dx.doi.org/
739 10.1016/j.rse.2018.03.010. doi:10.1016/j.rse.2018.03.010.

B. Cao, J.-P. Gastellu-Etchegorry, Y. Du, H. Li, Z. Bian, T. Hu, W. Fan, Q. Xiao, Q. Liu, Evaluation of four kernel-driven models in the thermal infrared band, IEEE Transactions on Geoscience and Remote Sensing 57 (2019) 5456–5475. URL: http://dx.doi.org/10.1109/TGRS.2019.2899600. doi:10.1109/tgrs.2019.2899600.

C. Duffour, J. P. Lagouarde, J. L. Roujean, A two parameter model to simulate thermal infrared directional effects for remote sensing applications, Remote Sensing of Environment 186 (2016) 250–261. URL: https://www.sciencedirect.com/science/article/pii/S0034425716303157. doi:10.1016/j.rse.2016.08.012.

K. Y. Vinnikov, Y. Yu, M. D. Goldberg, D. Tarpley, P. Romanov, I. Laszlo, M. Chen, Angular anisotropy of satellite observations of land surface temperature, Geophysical Research Letters 39 (2012) n/a–n/a. URL: http://dx.doi.org/10.1029/2012gl054059. doi:10.1029/2012gl054059.

P. C. Guillevic, A. Bork-Unkelbach, F. M. Gottsche, G. Hulley, J.-P. Gastellu-Etchegorry, F. S. Olesen, J. L. Privette, Directional viewing effects on satellite land surface temperature products over sparse vegetation canopies-a multisensor analysis, IEEE Geoscience and Remote Sensing Letters 10 (2013) 1464–1468. URL: http://dx.doi.org/10.1109/LGRS.2013.2260319. doi:10.1109/lgrs.2013.2260319.

H. Ren, R. Liu, G. Yan, X. Mu, Z.-L. Li, F. Nerry, Q. Liu, Angular normalization of land surface temperature and emissivity using multiangular middle and thermal infrared data, IEEE Transactions on Geoscience and Remote Sensing 52 (2014) 4913–4931. URL: http://dx.doi.org/10.1109/tgrs.2013.2285924. doi:10.1109/tgrs.2013.2285924.

J. B. Fisher, B. Lee, A. J. Purdy, G. H. Halverson, M. B. Dohlen, K. Cawse-Nicholson, A. Wang, R. G. Anderson, B. Aragon, M. A. Arain, et al., Ecostress: Nasa's next generation mission to measure evapotranspiration from the international space station, Water Resources Research 56 (2020) e2019WR026058.

768 G. Hulley, S. Hook, Ecostress level-2 lst and emissivity algorithm theoretical basis
769 document (atbd)(no. jpl d-94643), Jet Propulsion Laboratory, California Institute of
770 Technology (2018).

771 D. Roy, M. Wulder, T. Loveland, W. C.E., R. Allen, M. Anderson, D. Helder, J. Irons,
772 D. Johnson, R. Kennedy, T. Scambos, C. Schaaf, J. Schott, Y. Sheng, E. Vermote,
773 A. Belward, R. Bindschadler, W. Cohen, F. Gao, J. Hipple, P. Hostert, J. Huntington,
774 C. Justice, A. Kilic, V. Kovalskyy, Z. Lee, L. Lymburner, J. Masek, J. McCorkel,
775 Y. Shuai, R. Trezza, J. Vogelmann, R. Wynne, Z. Zhu, Landsat-8: Science and
776 product vision for terrestrial global change research, Remote Sensing of Environ-
777 ment 145 (2014) 154–172. URL: http://dx.doi.org/10.1016/j.rse.2014.
778 02.001. doi:10.1016/j.rse.2014.02.001.

779 S. J. Hook, J. J. Myers, K. J. Thome, M. Fitzgerald, A. B. Kahle, The modis/aster
780 airborne simulator (master)—a new instrument for earth science studies, Remote
781 Sensing of Environment 76 (2001) 93–102.

782 G. C. Hulley, S. J. Hook, E. Abbott, N. Malakar, T. Islam, M. Abrams, The aster global
783 emissivity dataset (aster ged): Mapping earth's emissivity at 100 meter spatial scale,
784 Geophysical Research Letters 42 (2015) 7966–7976. URL: http://dx.doi.org/
785 10.1002/2015GL065564. doi:10.1002/2015gl065564.

786 A. Berk, P. Conforti, R. Kennett, T. Perkins, F. Hawes, J. van den Bosch, Modtran6: a
787 major upgrade of the modtran radiative transfer code, in: Algorithms and Technolo-
788 gies for Multispectral, Hyperspectral, and Ultraspectral Imagery XX, 2014, p. nil.
789 URL: http://dx.doi.org/10.1117/12.2050433. doi:10.1117/12.2050433.

790 R. Gelaro, W. McCarty, M. J. Suárez, R. Todling, A. Molod, L. Takacs, C. A. Ran-
791 dles, A. Darmenov, M. G. Bosilovich, R. Reichle, K. Wargan, L. Coy, R. Cul-
792 lather, C. Draper, S. Akella, V. Buchard, A. Conaty, A. M. da Silva, W. Gu, G.-
793 K. Kim, R. Koster, R. Lucchesi, D. Merkova, J. E. Nielsen, G. Partyka, S. Paw-
794 son, W. Putman, M. Rienecker, S. D. Schubert, M. Sienkiewicz, B. Zhao, The
795 modern-era retrospective analysis for research and applications, version 2 (merra-2),

Journal of Climate 30 (2017) 5419–5454. URL: http://dx.doi.org/10.1175/JCLI-D-16-0758.1. doi:10.1175/jcli-d-16-0758.1.

N. K. Malakar, G. C. Hulley, S. J. Hook, K. Laraby, M. Cook, J. R. Schott, An operational land surface temperature product for landsat thermal data: Methodology and validation, IEEE Transactions on Geoscience and Remote Sensing 56 (2018) 5717–5735. URL: http://dx.doi.org/10.1109/TGRS.2018.2824828. doi:10.1109/tgrs.2018.2824828.

S. J. Hook, et al., HyspIRI Level-2 Thermal Infrared (TIR) land surface temperature and emissivity algorithm theoretical basis document., Technical Report, Pasadena, CA: Jet Propulsion Laboratory, National Aeronautics and Space . . . , 2011.

D. Hoese, P. Lahtinen, M. Raspaud, W. Roberts, Lavergne, S. Bot, G. Holl, S. Finkensieper, G. Ghiggi, A. Dybbroe, X. Zhang, M. Itkin, A. Meraner, BENR0, A. Valentino, Nina, L. Ørum Rasmussen, lorenzo clementi, M. Valgur, D. Rykov, A. Brammer, B. Hawkins, F. Pinault, storpipfugl, owenlittlejohns, A. R. P. Morena, B. Couwenberg, B. Esse, pytroll/pyresample: Version 1.26.0 post 0, 2022. URL: https://doi.org/10.5281/zenodo.7358887. doi:10.5281/zenodo.7358887.

L. Su, X. Li, M. Friedl, A. Strahler, X. Gu, Kernel-driven model of effective directional emissivity for non-isothermal surfaces, Progress in Natural Science 12 (2002) 603–607.

J.-P. Lagouarde, M. Irvine, Directional anisotropy in thermal infrared measurements over toulouse city centre during the capitoul measurement campaigns: First results, Meteorology and Atmospheric Physics 102 (2008) 173–185. URL: http://dx.doi.org/10.1007/s00703-008-0325-4. doi:10.1007/s00703-008-0325-4.

P. Virtanen, R. Gommers, T. E. Oliphant, M. Haberland, T. Reddy, D. Cournapeau, E. Burovski, P. Peterson, W. Weckesser, J. Bright, S. J. van der Walt, M. Brett, J. Wilson, K. J. Millman, N. Mayorov, A. R. J. Nelson, E. Jones, R. Kern, E. Larson, C. J. Carey, İ. Polat, Y. Feng, E. W. Moore, J. VanderPlas, D. Laxalde, J. Perktold,

R. Cimrman, I. Henriksen, E. A. Quintero, C. R. Harris, A. M. Archibald, A. H. Ribeiro, F. Pedregosa, P. van Mulbregt, A. Vijaykumar, A. P. Bardelli, A. Rothberg, A. Hilboll, A. Kloeckner, A. Scopatz, A. Lee, A. Rokem, C. N. Woods, C. Fulton, C. Masson, C. Häggström, C. Fitzgerald, D. A. Nicholson, D. R. Hagen, D. V. Pasechnik, E. Olivetti, E. Martin, E. Wieser, F. Silva, F. Lenders, F. Wilhelm, G. Young, G. A. Price, G.-L. Ingold, G. E. Allen, G. R. Lee, H. Audren, I. Probst, J. P. Dietrich, J. Silterra, J. T. Webber, J. Slavič, J. Nothman, J. Buchner, J. Kulick, J. L. Schönberger, J. V. de Miranda Cardoso, J. Reimer, J. Harrington, J. L. C. Rodríguez, J. Nunez-Iglesias, J. Kuczynski, K. Tritz, M. Thoma, M. Newville, M. Kümmerer, M. Bolingbroke, M. Tartre, M. Pak, N. J. Smith, N. Nowaczyk, N. Shebanov, O. Pavlyk, P. A. Brodtkorb, P. Lee, R. T. McGibbon, R. Feldbauer, S. Lewis, S. Tygier, S. Sievert, S. Vigna, S. Peterson, S. More, T. Pudlik, T. Oshima, T. J. Pingel, T. P. Robitaille, T. Spura, T. R. Jones, T. Cera, T. Leslie, T. Zito, T. Krauss, U. Upadhyay, Y. O. Halchenko, Y. Vázquez-Baeza, S. . Contributors, Scipy 1.0: Fundamental algorithms for scientific computing in python, Nature Methods 17 (2020) 261–272. URL: http://dx.doi.org/10.1038/s41592-019-0686-2. doi:10.1038/s41592-019-0686-2.

N.-E. Tsendbazar, A. Tarko, L. Li, M. Herold, M. Lesiv, S. Fritz, V. Maus, Copernicus Global Land Service: Land Cover 100m: version 3 Globe 2015-2019: Validation Report, 2021. URL: https://doi.org/10.5281/zenodo.4723975. doi:10.5281/zenodo.4723975.

F. Kriegler, W. Malila, R. Nalepka, W. Richardson, Preprocessing transformations and their effects on multispectral recognition, Remote sensing of environment, VI (1969) 97.

R. Niclòs, J. Puchades, C. Coll, M. J. Barberà, L. Pérez-Planells, J. A. Valiente, J. M. Sánchez, Evaluation of landsat-8 tirs data recalibrations and land surface temperature split-window algorithms over a homogeneous crop area with different phenological land covers, ISPRS Journal of Photogrammetry and Remote Sensing 174 (2021) 237–253. URL: http://dx.doi.org/10.1016/j.isprsjprs.2021.02.005. doi:10.1016/j.isprsjprs.2021.02.005.

D. Phiri, M. Simwanda, S. Salekin, V. R. Nyirenda, Y. Murayama, M. Ranagalage, Sentinel-2 data for land cover/use mapping: A review, Remote Sensing 12 (2020) 2291.

J.-P. Lagouarde, A. Hénon, B. Kurz, P. Moreau, M. Irvine, J. Voogt, P. Mestayer, Modelling daytime thermal infrared directional anisotropy over toulouse city centre, Remote Sensing of Environment 114 (2010) 87–105. URL: http://dx.doi.org/10.1016/j.rse.2009.08.012. doi:10.1016/j.rse.2009.08.012.

L. Jiang, W. Zhan, L. Hu, F. Huang, F. Hong, Z. Liu, J. Lai, C. Wang, Assessment of different kernel-driven models for daytime urban thermal radiation directionality simulation, Remote Sensing of Environment 263 (2021) 112562. URL: http://dx.doi.org/10.1016/j.rse.2021.112562. doi:10.1016/j.rse.2021.112562.

J. Michel, O. Hagolle, S. J. Hook, J.-L. Roujean, P. Gamet, Master and Landsat-8 simultaneous acquisition datacubes for the quantification of directional anisotropy in Thermal Infra-Red domain, 2023. URL: https://doi.org/10.5281/zenodo.7757028. doi:10.5281/zenodo.7757028.

## List of Figures